BioNanoScience (2026) 16:391
https://doi.org/10.1007/s12668-026-02638-x

RESEARCH

AI-Enhanced Design of Nitro-Pyrimidine-Loaded SLNs: Integrating Molecular Modeling, and Biological Characterization for Cancer Therapy

Dillibabu Krishnan[1] · Priya Manogar[1,3] · Panneerselvam Theivendren[2]

Received: 11 March 2026 / Accepted: 21 May 2026

Abstract

Breast cancer remains one of the leading causes of cancer-related death in the world, and there is a great need for the development of new advanced targeted therapeutic techniques with higher efficiency and lower systemic toxic effects. The present study was directed towards the development and biological evaluation of novel nitro pyrimidine loaded solid lipid nanoparticles (SLNs) as a targeted anticancer drug delivery system with the aid of artificial intelligence. Ligand D14, which was identified as the most promising TACE inhibitor by the machine learning-based bioactivity prediction algorithm, exhibited the most favorable docking score of −9.4 kcal/mol and stable molecular interactions in 100 ns of molecular dynamics simulations. The optimized formulation of SLN showed good encapsulation efficiency (91.00 ± 2.3%) and the capacity of drug loading (9.01 ± 0.8%) which signified successful incorporation of the nitro-pyrimidine derivative in the lipid matrix. The *in vitro* drug-release assays showed that the cumulative drug-release percentage was 93.1% at pH 7.8 and 74.3% at pH 5.2 after 75 h. Structural integrity, crystallinity, nanoscale particle distribution and formulation stability were confirmed by physicochemical characterization via FTIR, XRD, LC-MS, FE-SEM, and particle-size analysis. Biological assays performed in the breast cancer cells (MCF-7) showed substantial dose-dependent cytotoxicity and apoptosis induction, especially at 100 µg/mL. Altogether, the results indicate that AI-supported nitro-pyrimidine loaded SLNs are a potential promising targeted nanotherapeutic platform for breast cancer management as translatable in precision oncology.

Keywords Solid lipid nanoparticles · Pyrimidine derivatives · Drug delivery systems · Breast cancer · Cytotoxicity · Encapsulation efficiency

1 Introduction

Purines of a type of nitrogen bases are not the only ones detected in nucleic acids as the other one is pyrimidines. They are a constituent part of both the DNA and the RNA, and an essential part of the cell operation, they are a type of genetic information, the process of transcription and the creation of proteins [1]. The pyrimidines are characterized by a six-membered ring, having a nitrogen atom at the first and third position and formed by cytosine (C), thymine (T) and uracil(U) that are essential parts of nucleic acids. In addition to their structural role in the nucleic acids, pyrimidines also have various metabolic processes like in the manufacture of coenzymes like UDP-glucose and ATP that are fundamental in energy metabolism [2, 3]. The role of pyrimidines in

✉ Priya Manogar
priyamanokhar@gmail.com

1 Department of Chemistry, School of Basics Sciences, Vels Institute of Science, Technology & Advanced Studies, Pallavaram, Chennai, Tamil Nadu 600117, India

2 Department of Pharmaceutical Chemistry & Analysis, School of Pharmaceutical Sciences, Vels Institute of Science, Technology & Advanced Studies, Pallavaram, Chennai, Tamil Nadu 600117, India

3 Department of Chemistry, School of Basics Sciences, VISTAS, Pallavaram, Chennai, Tamil Nadu 600 117, India

Published online: 29 May 2026

biology is not limited to using the compounds in genetic material. They are also linked to a number of biosynthetic pathways such as in cell cycle and manufacture of neurotransmitters. Pyrimidines have also been found to have been active agent in various treatment environments especially in curing cancer, viral infections and autoimmune diseases. Their clinical medicine is 5-fluorouracil (5-FU), azidothymidine (AZT) pyrimidine analogues have been much used in chemotherapy and as antiviral therapy respectively [4–6]. Furthermore, the pyrimidines are found in cell-based signalling in various metabolites. For one example, UDP-glucose is one of the products of pyrimidine metabolism; it plays an important role in glycosylation reactions, which can influence the function of proteins, the signalling of receptors and cell communication. The control of pyrimidine metabolism is also highly regulated and the feedback mechanism ensures an equilibrium between supply and demand of pyrimidines and the homeostatic regulation is of great importance to maintain the normal functioning of the cells [7–9]. Solid liquid nanoparticles (SLNs) are one of the recent advancements in the pharmaceutical science used as drug delivery carrier. Some advantages of lipid matrix based SLNs are biocompatibility, slow release and simplicity of preparation. SLNs with individual Pyrimidine-based drug have a potential of higher bioavailability and target efficacy and lower systemic toxicity [10–12]. To achieve a therapeutic effect for an extended period of time, Pyrimidine analogues release profile can also be modified with the help of SLNs. As pyrimidines is a biomedicine and the SLN technology has potential to maximise pyrimidine, one can suggest pyrimidines/SLN technology as an effective approach of increasing the efficacy of pyrimidine-based medicine. High potential of the strategy in diseases where localised and controlled delivery is essential in optimization of therapy such as treatment in various diseases like cancer, viral and neurological diseases [13–15].

This study is present the biological significance of the pyrimidine derivatives as well as explore the opportunities that the solid lipid nanoparticles (SLNs) have in enhancing the delivery of pyrimidine-based drug. The target of the work is assessment of development of the pyrimidine-based drug in SLNs, properties of pyrimidine drug release, bioavailability, therapeutic efficiency. The interaction of the pyrimidine drug-lipid matrix as well as its stability, *in vivo* target effectiveness and cytotoxicity will be tested in the paper. It is this paper that will be contributing to the development of more effective drug delivery systems which will be encompassing pyrimidines and SLN technology to ensure that pyrimidine-based drug compounds can be used effectively in medicine, for example in cancer and viral infections. If such an approach is taken, the research will provide a foundation for the use of SLNs in the future in clinical practice for the treatment of pyrimidine drugs. The present work is distinguished from other applications of solid lipid nanoparticles (SLNs) as a drug delivery system, but does not rely exclusively on the SLN technology. This study aims to prove the central hypothesis that the rationally designed nitro-substituted pyrimidine derivative delivered by a cetylpalmitate SLN efficiently blocks the activity of the shedding enzyme, which in turn, is involved in the shedding of HER2 and progression of breast cancer, upon reaching the tumour microenvironment at low pH. Novelty of this study is the three explicit elements that have not been combined for this target: (i) machine-learning based prioritisation of TACE inhibitors based on BindingDB and an external set of 3,108-compound phytochemicals, (ii) molecular docking and 100-ns molecular-dynamics confirmation of the prioritised ligand (D14) on the crystal structure of TACE (3EWJ), and (iii) experimental SLN formulation, biophysical characterisation and MCF-7 cytotoxicity and apoptosis evaluation of the prioritised compound. Specific aims are, therefore, to (a) develop and validate a Random Forest model for the prediction of TACE bioactivity, (b) develop a 25-compound TACE targeted library of ligands and rank them computationally, (c) design and characterize the lead TACE-targeted SLNs, and (d) quantify pH-dependent release, cytotoxicity, and apoptotic mechanism in MCF-7 cells.

2 Methodology

2.1 Dataset Acquisition

The information used in this study was found on the BindingDB database, and the special attention was paid to the compounds that have been reported to interact with TACE. The entries included identifiers of the monomers, molecular representations in the SMILES (Simplified Molecular Input Line Entry System) format, and experimental values of IC_{50} in nanomoles (nM). To facilitate quantitative modelling, the values of the IC_{50} were converted to their negative logarithmic form (pIC_{50}) in order to make the measurements of the activity more consistently and interpretable. Structural validation was done to guarantee chemical soundness in the dataset and exclude the chemical compounds with improper or inconsistent SMILES descriptions with the cheminformatics libraries (RDKit and Open Babel). A large number of molecular descriptors of both structural and physicochemical properties were then produced through the Mordred descriptor calculator. Based on pIC_{50} thresholds, compounds were stratified into three categories: inactive or least active ($pIC_{50} \leq 5.0$), moderately active ($5.0 < pIC_{50} \leq 7.5$), and highly active ($pIC_{50} > 7.5$) [16].

2.2 Data Processing and Feature Selection

A preprocessing pipeline was conducted with the initial dataset of descriptors that was aimed at maximising the quality of features to be used in machine learning. A systemic removal of descriptors with missing or null values was done to ensure the integrity of the data. A constant-value filter was used to drop features which had no variance, whereas those with extremely low variance (less than 0.01) were dropped because they lacked discriminatory ability. In order to minimise redundancy and multicollinearity in the dataset, descriptors with Pearson correlation coefficient above 0.75 were eliminated. Outliers were detected and removed using a Z-score cutoff of ±7 so that model training was not distorted. Variable-importance measures were then used to rank the refined set of descriptors and the most informative features were chosen for further modelling. The cleaned dataset was partitioned into training and internal-validation subsets in a 70:30 stratified split, and a separate external test set comprising 3,108 phytochemical compounds (downloaded from the IMPPAT and CMAUP natural-product databases) was held out to provide unbiased external validation of the final classifier, in line with OECD QSAR principle 4 [17, 18].

2.3 Model Development

The entire set of machine learning models was developed to identify the bioactivity of TACE-targeting compounds. The algorithms that were chosen included the Random Forest, Instance-Based k-Nearest Neighbour (IBK), Multilayer Perceptron, Decision Tree, Logistic Regression, Sequential Minimal Optimization (SMO) and Naive Bayes. All the implementations of the models were made through the WEKA platform that provides powerful classification and data mining tools. Models were evaluated in terms of several measures of performance such as accuracy, Cohen Kappa statistic, Mean Absolute Error (MAE), Root mean squared error (RMSE), Relative Absolute Error (RAE) and root relative squared error (RRSE). In order to stabilise the model and guarantee that the results are generalised, a 10-fold cross-validation process was added to the regular training-test split [19].

2.4 Compound Library Design

The rationally designed library of 25 novel ligands that are selective against TACE was discussed in this study, based on what is known about pharmacophores and structure-activity relationship (SAR) analysis. Chemical structures of these ligands were carefully built and optimised with cheminformatics software programmes like RDKit and Open Babel with proper 3D conformer generation and reliable determination of molecular descriptors. The designed machine learning models used this custom-designed ligand library as their input to predict the bioactivity profiles against TACE. Predicted active compounds were selected as targets of further computational validation, such as molecular docking and molecular dynamics simulations, to determine their binding affinity, interaction stability and specificity to TACE target hence aiding in the identification of promising targets to be experimented [20].

2.5 Network Pharmacology

The elaborate interplay between medicines and disorders is a complex matter that can be studied in a complex multidimensional way to be called network pharmacology. In the research, the use of advanced software in network pharmacology was presented, and bioactive Stigmasterol was investigated through Stitch software and Swiss Target Prediction. Such tools aided in setting potential target of Stigmasterol particularly breast cancer. The targets were profiled and were screened using DiseNET to obtain information on the therapy role which could be played by Stigmasterol. To analyse its molecular properties, a number of structural and functional analyses were performed by ChemDraw, PyMOL, and Swiss ADME. These programmes helped in isolating some of the major properties of Stigmasterol including its molecular properties and its potential therapeutical application. Another example of the role played by the protein 3EWJ (TACE), which is associated with breast cancer, was also explored in more detail thanks to the application of Cytoscape and STRING that allowed to consider the influence of the aforementioned protein on cancer pathways and other related processes in greater detail. This current review paper identifies the opportunities of Stigmasterol as a promising candidate agent in managing cancer because it targets certain cancer pathways, which have been determined through computational tools [3, 21, 22].

2.6 Protein Analysis

Protein structure has a close relationship with their roles and the structure integrity may be very significant in bioactivity of a protein. The Ramachandran plot produced by the PROCHECK tool availed by the European Bioinformatics Institute (EBI) indicated the effectiveness of the protein structure of 3EWJ (TACE) in this research study. Ramachandran plot scores on steric quality of the protein structure i.e. the extent to which the protein has the optimum value of the dihedral angles. It helps in determining the region where conformational stability within the protein occurs and the region that has deviation of values. Per-formation of G-factors analysis

which are significant elements in the entire stability of the protein and its functionality was also done. The bonds and residues geometrical distribution and length of the bonds was also studied so as to have an additional confidence of the integrity of the protein structure. The fundamental nature of the biological behaviour of the protein and the potential therapeutic application are based on this critical analysis of the structural stability of the protein [21, 22].

2.7 Molecular Docking Analysis

Molecular docking is a good computational technique which provides a clue on the arrangement of binding of the ligands and the proteins they aim to bind. This study was carried out by the application of the molecular docking process by exploring the interaction of various ligands with 3EWJ (TACE) protein. This has been implemented by altering the structure of the proteins by removal of the water molecules and addition of polar atoms into the molecule with more bonding interactions. Ligand preparation had been prepared and docking grid box had been fixed such that all the potential binding sites of the protein had been incorporated. AutoDock Vina was used to conduct docking simulations and the obtained interactions between the ligands and the protein were taken into consideration. The objective of such docking analysis exercise was to ensure that indeed the ligands binding in the active binding position of the 3EWJ protein and hence the potentiality of such ligands as the therapeutic ones. This form of calculation provides valuable data on the way that individual ligands can be exploited to control the functions of the proteins, and allows the development of the particular remedies [3, 23].

2.8 Molecular Dynamics Analysis

Molecular dynamics (MD) is a computational technique for observing the dynamics of protein-ligand interactions over time and under varying physiological conditions. In the present work, MD simulations were performed in Schrödinger Desmond (Maestro 2021-2, Schrödinger LLC, NY, USA) to follow the behaviour of the 3EWJ (TACE)-ligand complex. The simulation environment was set to mimic physiological conditions, including the addition of TIP3P water molecules and Na^+/Cl^- ions to maintain electrical neutrality. Temperature (300 K) and pressure (1.013 bar) were equilibrated and the simulation time was set at 100 ns to ensure that the system responded to physiological conditions. An NPT-ensemble simulation was used to measure the flexibility and stability of the protein-ligand system over time, based on the dynamics of the atoms and molecules in the system. The structural stability and dynamic behaviour of the complex were monitored through the calculation of major parameters such as Root Mean Square Deviation (RMSD) and Root Mean Square Fluctuation (RMSF). These metrics provide insights on the consistency of the protein-ligand interaction, which is a vital parameter in evaluating the therapeutic worth of the compound [24, 25].

2.9 ADMET Analysis

It has state-of-the-art programmes known as ADMETlab 3.0 which are used to predict the ADMET (Absorption, Distribution, Metabolism, Excretion, and Toxicity) of small molecules, which provides information on the nature of their pharmacokinetics. The platform is based on machine-learning algorithms and curated databases that assess the most significant aspects, including intestinal permeability, blood-brain barrier penetration, cytochrome P450 enzyme interactions, and potential toxicity. Researchers may submit compound structures in various formats (SMILES, InChI, MOL) or draw them on the site. Once a structure is uploaded, a comprehensive evaluation of the pharmacokinetic and safety profile of the compound is performed by ADMETlab 3.0. These findings are presented as scores and graphs that allow researchers to consider the drug-likeness and safety of their compounds. This tool plays a pivotal role in drug discovery in that early evaluation of the pharmacology of putative therapeutic agents is performed [26, 27].

2.10 HOMO and LUMO Analysis

Density Functional Theory (DFT) is a quantum-mechanical framework that is utilised to explore the electronic structure of molecules and provides vital information on the stability and reactivity of molecules. This paper applies DFT to investigate the electronic properties of the lead compound. The information was retrieved from PubChem, and Spartan 14 software was used for energy optimisation. Calculation of the Highest Occupied Molecular Orbital (HOMO) and the Lowest Unoccupied Molecular Orbital (LUMO) was performed with the help of GaussView 6.0.16. The energy difference between HOMO and LUMO is the primary marker of the electronic properties of a compound, particularly its reactivity and stability. The information obtained is important for understanding the potential of the compound as a therapeutic agent and its performance under diverse chemical conditions [3].

2.11 Formulation of Nitro-Pyrimidine SLNs

The synthesis of the nitro-pyrimidine loaded SLNs was done by utilising a mixture of ultrasonic treatment and high-speed mixing technique. Formulation process was carried out by dissolving cetyl palmitate in diethyl ether

at which point heating was done to obtain a homogenous lipid phase. Ultrasonication of the drug-lipid mixture was done to create a stable microemulsion. This was done by the use of a dual surfactant in the form of polysorbate-80 and sodium deoxycholate that stabilised the formulation to give a clear and thermodynamically stable colloidal system. The ultracentrifugation was then applied on the SLN suspension at 10,000 rpm to allow a further separation and purification of the particles. The performance of the formulation was evaluated quantitatively through the determination of drug loading capacity and encapsulation efficiency through known methods of analysis which showed the success of SLNs as a drug delivery vehicle of nitro-pyrimidine. To further optimise our product, we put through samples of the SLNs through the ultracentrifugation process at 10,000 rpm, which tremendously optimally separated and purified our formulation. Our performance criteria were then used to determine the performance of our system by determining the drug loading capacity and encapsulation efficiency by using the established pharmaceutical equations.

2.12 *In vitro* drug Release Analysis

drug release *in vitro* was done by dialysis bag diffusion technique with a cutoff molecular weight of 3,500 Da. The nitro-pyrimidine-loaded SLNs were tested with the under physiologically relevant conditions by release media at different pH value (acetate buffer pH 5.0 and phosphate buffer pH 7.8) at 37 °C. Quantification of drug release was carried out by High-Performance Liquid Chromatography (HPLC). Analyses were performed on a Shimadzu Prominence-i LC-2030 C 3D Plus system (Shimadzu Corporation, Kyoto, Japan) fitted with a Phenomenex Luna C18 column (4.6 × 250 mm, 5 µm) using an isocratic mobile phase of acetonitrile-water (60:40 v/v) at 1.0 mL/min and PDA detection at 268 nm; LabSolutions v5.97 software was used for peak integration. This approach made it possible to fully characterise the sustained-release kinetics, demonstrating the ability of SLNs to deliver the drug over a prolonged period.

2.13 Kinetics Release Analysis

Several mathematical models were used to study the drug release mechanism such as zero-order, first-order, Higuchi, Korsmeyer-Peppas, and Hixson-Crowell models. The result of this in-depth kinetic analysis was the ability to calculate the rate and the mechanism of release of nitro-pyrimidine discussed in the SLN matrix. The kinetic analysis was of essential interest with regards to optimization of formulations and the creation of a controlled release profile that is able to sustain therapeutic drug levels over longer periods of time in order to increase the clinical potential of nitro-pyrimidine therapy.

2.14 Stability Analysis

Systematic assessment of the stability of the nitro-pyrimidine-loaded SLNs in different physiological conditions was done. Stability testing was done in various media such as sodium chloride solution, bovine serum albumin (BSA), acetate buffer and phosphate buffer at temperature of 37 °C and in pH of 5.0 and 7.8. The stability of SLN because of the influence of UV-visible spectrophotometry was observed based on the shift in absorbance (λmax) values. This method of analysis yielded useful information about the integrity of the structure of the SLNs compared to their ability to sustain stability of nitro-pyrimidines when exposed to various physiological conditions. The findings proved that the SLN formulation was structurally intact and was able to keep the encapsulated nitro-pyrimidine intact to use in therapeutic uses.

2.15 LC-MS Analysis

The integrity and stability of the encapsulated nitro-pyrimidine in the SLN matrix was checked using Liquid Chromatography-Mass Spectrometry (LC-MS). Analyses were performed on a Waters Acquity UPLC H-Class system coupled to a Waters Xevo G2-XS QTof mass spectrometer (Waters Corporation, Milford, MA, USA) operated in positive electrospray-ionisation mode (capillary 3.0 kV; cone 30 V; source 120 °C; desolvation 350 °C). Chromatographic separation was achieved on an Acquity BEH C18 column (2.1 × 100 mm, 1.7 µm) using a 0.1% formic acid/acetonitrile gradient at 0.3 mL/min, and data were processed in MassLynx v4.2. The LC-MS findings proved successful encapsulation without any traces of drug degradation or loss during the formulation procedure. The spectral data confirmed that the encapsulated compound remained stable, demonstrating that the molecular integrity of nitro-pyrimidine was maintained throughout SLN preparation.

2.16 FTIR Analysis

The FTIR spectroscopy was used to study the molecular interactions between the SLN lipid matrix and nitro-pyrimidine. A Shimadzu IR Tracer-100 was used to do spectral analysis between the range of wavenumbers of 400–4000 cm^{-1}. The FTIR test was done to find out the main functional groups in the encapsulation process and the study ensured there was compatibility between nitro-pyrimidine and the lipid components. The spectroscopic evidence showed that the molecular level compatibility

was observed and that the structural integrity of nitro-pyrimidine was also maintained during the formulation of the encapsulation.

2.17 X-Ray Analysis

Nitro-pyridine solid lipid nanoparticles were analysed through X-ray diffraction with the use of an X-ray diffractometer at 40 kV and 40 mA under Cu Ka radiation with the wavelength of 1.5418 Å. A series of scans on a 2θ range of 10-90^{o} was applied to the samples to get the diffractogram with crystallographic structures and intensities of the peaks. The resulting patterns of diffraction were examined in order to determine the number of discrete peaks and the Miller indices associated with each peak and the relative intensities of the peaks calculated in counts. In the case of the analysis of the energy dispersive X-ray spectroscopy, the samples of the nanoparticle were analysed concerning an energy range of 0–10 keV in order to analyse the elemental composition. In order to determine characteristic peaks of carbon, hydrogen and oxygen elements, the EDX spectrum was obtained and their energy level and strength of peaks were measured in pixels/electron. The spectral data was assessed to determine elemental distribution and the relative abundance of the various constituents in the formulation and also to determine the existence of any contaminants or heavy metal impurities.

2.18 FE-SEM Analysis

The morphology and size distribution of the nitro-pyrimidine-loaded SLNs were characterised by Field Emission Scanning Electron Microscopy (FE-SEM). Imaging was carried out on a Carl Zeiss Sigma 300 FE-SEM (Carl Zeiss Microscopy GmbH, Oberkochen, Germany) operated at an accelerating voltage of 5 kV using the in-lens secondary-electron detector. Lyophilised SLN powder was redispersed in distilled water, drop-cast onto a clean silicon wafer, vacuum-dried, and sputter-coated with a 5-nm gold layer using a Quorum Q150R ES sputter coater prior to imaging. The FE-SEM imaging was used to visualise the morphology of the SLNs and to assess particle uniformity and structural stability. The microscopic examination confirmed the appropriateness of the developed SLNs as drug-delivery vehicles and supported their use in controlled drug-delivery systems.

2.19 Particle Size Analysis

The hydrodynamic particle size, polydispersity index (PDI), and zeta potential of the nitro-pyrimidine-loaded SLN dispersion were determined by dynamic light scattering (DLS) using a Malvern Zetasizer Nano ZS90 (Malvern Panalytical Ltd., Malvern, UK) equipped with a 4 mW He-Ne laser (λ = 633 nm) at a fixed scattering angle of 90°. The freshly prepared SLN suspension was diluted 100-fold with 0.22 µm-filtered double-distilled water to avoid multiple-scattering effects, equilibrated for 120 s at 25 ± 0.1 °C, and analysed in triplicate disposable polystyrene cuvettes (DTS0012). Each measurement consisted of three runs of 13 sub-runs and the size distribution was reported as the intensity-weighted mean diameter (Z-average). Zeta potential was measured in disposable folded capillary cells (DTS1070) by laser Doppler micro-electrophoresis under the Smoluchowski approximation. All values are reported as mean ± SD of three independently prepared batches.

2.20 MTT Assay

The cytotoxic activity of nitro-pyrimidine-SLNs was determined by the MTT test on the MCF-7 breast cancer cells. The cells were cultured in DMEM medium with foetal bovine serum and penicillin- streptomycin at a normal atmosphere. Different concentrations of nitro-pyrimidine impregnated SLNs were added to the cultures of cells and incubated overnight with 37 °C. The viability of the cells was measured with MTT reagent and absorbance was taken at a wavelength of 570 nm to determine the effect of cytotoxicity. The obtained results of MTT assay contained the necessary biocompatibility information, and showed the anticancer activity of the nitro-pyrimidine-containing SLNs. Such results underpin the possible use of such formulation in the treatment regimens of cancer.

2.21 Fluorescence Microscopy Analysis

MCF-7 breast-cancer cells were seeded at 1×10^5 cells/well on poly-L-lysine-coated glass coverslips placed in 6-well plates and allowed to adhere overnight at 37 °C in a humidified 5% CO_2 atmosphere. After reaching 70–80% confluency, cells were treated with rhodamine-B-tagged nitro-pyrimidine SLNs at concentrations of 6.25, 12.5, 25, 50, and 100 µg/mL for 24 h, while untreated wells served as controls. After incubation, cells were washed thrice with ice-cold phosphate-buffered saline (PBS, pH 7.4), fixed with 4% paraformaldehyde for 15 min at room temperature, and the nuclei counter-stained with 4′,6-diamidino-2-phenylindole (DAPI; 1 µg/mL) for 10 min. Coverslips were mounted in fluoromount aqueous medium and observed under an inverted fluorescence microscope (Olympus IX73, Olympus Corporation, Tokyo, Japan) equipped with appropriate excitation/emission filter cubes (DAPI: 358/461 nm; rhodamine: 540/625 nm). Digital images were captured at 20× and 40× magnifications using a CCD camera, and fluorescence-intensity profiles were quantified in arbitrary units

(a.u.) using ImageJ v1.53 (NIH, Bethesda, MD, USA) on at least five randomly chosen fields per concentration.

2.22 Flow Cytometry Apoptosis Analysis

Cells were placed in 6-well plates with 2×10^5 cell/well and left to adhere overnight. When the cells had reached the necessary confluency, nitro-pyrimidine solid lipid nanoparticles were added to the cells at the IC50 concentration and at 100 µg/mL, and the control wells were not treated. After 24 h of incubation, cells were trypsinised, centrifuged at 1500 rpm for 5 min, and washed twice with cold PBS. Cell pellets were resuspended in 1× binding buffer at 1×10^6 cells/mL. Of every sample, 100 µL of cell suspension was moved into the flow cytometry tubes and was stained with 5 µL of Annexin V-FITC and 5 µL of propidium iodide as indicated by the manufacturer. Samples were swirled carefully and left to incubate in the dark at room temperature in 15 min. After incubation, 400 µL of binding buffer was put to each tube. Flow cytometric analysis was immediately done by using flow cytometer with 488 nm excitation laser. One sample obtained at least 10,000 events. The data analysis was performed with the help of corresponding software to measure the population of cells in four quadrants, which arrived at viable, early apoptotic, late apoptotic, and necrotic cells according to the patterns of fluorescence of Annexin V-FITC and PI.

3 Results and Discussion

3.1 Comparison of Machine Learning Models to Predict TACE Bioactivity

It was shown that the predictive performance of various machine learning models was thoroughly compared to categorise the bioactivity of compounds against TNF-α Converting Enzyme (TACE; ADAM17), a key sheddase implicated in inflammation, angiogenesis, and breast-cancer progression. In the model training, Random Forest (RF) was the most successful algorithm, with the high accuracy of 88.10% and Kappa statistic of 0.8200, which proves that they agreed well beyond the probability of accident. RF model also had minimal prediction error whereby the mean absolute error (MAE) was 0.1640 and root mean square error (RMSE) was 0.2500 indicating that the model was quite accurate in classifying bioactive compounds. There were other models like K-Star, Multilayer Perceptron (MLP), Instance-Based k-Nearest Neighbour (IBK) and Decision Tree (J48) which were also very reliable predictive models with the accuracy scores ranging between 80.20 and 92.64 and Kappa scores of between 0.7000 and 0.8895. On the other hand, the Logistic Regression, Sequential Minimal Optimization (SMO) and Naive Bayes exhibited rather lower values of accuracies and higher error rates, which means that this dataset can be classified with relatively lower accuracy. In order to confirm the soundness and usefulness of the model, the optimised Random Forest classifier was additional tested on a separate data of 3,108 phytochemical compounds, at this point, the classifier attained an accuracy of 72.30 and Kappa value of 0.4385, which denotes reasonable predictive capability on unobserved data. The MAE of 0.3478 and the RMSE of 0.4472 help further underline acceptable margins of errors in prediction, which indicates the possibility of the applicability of the model in the case of virtual screening and prioritisation of prospective TACE inhibitors. These results demonstrate the usefulness of Random Forest in predicting bioactivity and its possible use as a part of drug discovery programmes against TACE.

3.2 Choice of the Molecular Descriptors to use in Predicting TACE Inhibitors

The variables were carefully selected via variable importance analysis to find a set of 20 molecular descriptors that achieve optimal predictive modelling of biological activity of compounds against TACE. These descriptors cover a broad spectrum of molecular properties that are important to know and predict the interactions of the ligands with TACE. Among them are physicochemical descriptors like LogS to predict lipophilicity of a compound and molecular weight-related parameters (MW, MWC09, TMWC10) to determine the impact on pharmacokinetics and binding affinity. Spatial absorption coefficients (SpAbsA, SpAbsDzZ, SpAbs_Dzpe) give information about the distribution and conformational flexibility of molecules in three-dimensional space, which is necessary in complementary interactions with the TACE binding site. Autocorrelation descriptors (ATS0dv, ATS1dv, ATS0s, ATS1d, AATS0s) describe the spatial distribution of the atomic properties over the molecular graph, which captures both electronic and geometrical features of important molecular recognition. Topological and path-based indices are MID, Zagreb2, SRW04, SRW06, SRW08 and TSRW10 which measure molecular connectivity and shape and help to understand structural complexity and they can be possible hotspots of interaction. Also, WPol and nAromAtom descriptors report about the polarity of the molecule and the number of aromatic atoms, which is one of the main determinants of bioavailability and specificity of the receptor binding. The combination of this highly diverse and complementary set of descriptors permits a richer molecular representation, which increases predictive performance and strength of machine learning in the discovery of potent TACE inhibitors. This strategy can be used to discover and

rationally design new angiogenesis-related disease therapeutic agents.

3.3 Bioactivity of Designed Compounds Prediction

The 25 rationally designed compounds that were tested with the modelled Random Forest optimised model were 18 times predicted with confidence as "active" against TACE. The potentials of these compounds being effective inhibitors are promising and they should be investigated further using in silico studies like the studies that have been proposed which include molecular docking and molecular dynamics simulations. These studies will make them understand their binding affinities, stability of interaction and specificity to the TACE receptor, which will allow them to be prioritised later in experimental validation and drug development Tables 1, 2, 3 and 4; Figs. 1, 3, 3, 4 and 5.

3.4 Network Pharmacology

Network analysis of the protein-protein interactions indicated the characteristic patterns of centrality of the cancer related genes and three genes exhibited outstanding network significance. TACE, PTEN, and TP53 became the most central nodes with the same and largest centrality scores in each of the various measures (degree = 49, betweenness = 19.89, closeness = 0.0204, eigenvector = 0.167, radiality = 2, stress = 456). This intersection implies that these proteins are important regulatory centres of cancer pathways, which may be important drug targets because of their comprehensive connectivity and impact in the network topology.

The second level of hub protein was CDKN2A, BRCA1, KRAS, and SMAD4 all of which have high degree centrality (47–48 connexions) but with a slight difference in betweenness centrality values. It is important to note, that KRAS showed significantly lower betweenness centrality (16.76) than CDKN2A (18.29) and BRCA1 (17.70) and, therefore, plays a dissimilar role in the information flow in the network, despite the fact that they all had the same connectivity. The values of the eccentricity were maintained at 0.5 in most of the nodes except the first three hubs indicating the presence of well-connected network structure with short path lengths between two nodes.

Table 2 Performance comparison of six classification models based on accuracy, Kappa statistic, mean absolute error (MAE), root mean square error (RMSE), relative absolute error (RAE), and root relative squared error (RRSE)

Actual \ Predicted	Moderately Active	Active	Least Active
Actual: a (Moderately Active)	1145	335	94
Actual: b (Active)	320	865	57
Actual: c (Least Active)	85	50	157

Table 3 Performance comparison of six classification models based on accuracy, Kappa statistic, mean absolute error (MAE), root mean square error (RMSE), relative absolute error (RAE), and root relative squared error (RRSE)

Metric	Value
Correctly Classified Instances	2248 (72.30%)
Incorrectly Classified Instances	860 (27.70%)
Kappa Statistic	0.4385
Mean Absolute Error (MAE)	0.3478
Root Mean Squared Error (RMSE)	0.4472

Table 4 Performance comparison of six classification models based on accuracy, Kappa statistic, mean absolute error (MAE), root mean square error (RMSE), relative absolute error (RAE), and root relative squared error (RRSE)

Step	Descriptors Removed	Descriptors Remaining
Initial Descriptors	–	1800
NaN/Blank Filter	187	1613
Constant Filter	227	1386
Low Variance Filter	303	1083
High Correlation Filter	688	395
Z-score Filter	181	214
Variable Importance Selection	194	20

The proteins with lower-level, including CTNNB1, AKT1 and NRAS, were found to have lower centrality indices, especially betweenness and stress values, which means that they occupied more peripheral positions in the network. Nevertheless, they are included in the network, which implies their functional relevance in cancer biology, and it may have specialised functions in particular pathways. The values of the radialities steadily declined on the way towards the central to peripheral nodes in

Table 1 Performance comparison of six classification models based on accuracy, Kappa statistic, mean absolute error (MAE), root mean square error (RMSE), relative absolute error (RAE), and root relative squared error (RRSE)

Model	Accuracy (%)	Kappa	MAE	RMSE	RAE (%)	RRSE (%)
Random Forest	88.10	0.8200	0.1640	0.2500	36.50	53.00
Decision Tree	80.20	0.7000	0.1450	0.3400	32.50	72.50
Logistic Regression	44.50	0.1500	0.4200	0.4550	94.00	96.50
Multilayer Perceptron	53.00	0.2900	0.3600	0.4300	80.00	91.00
SMO	43.75	0.1500	0.3950	0.4950	89.00	105.00
Naive Bayes	44.70	0.1650	0.3850	0.4850	87.00	103.50

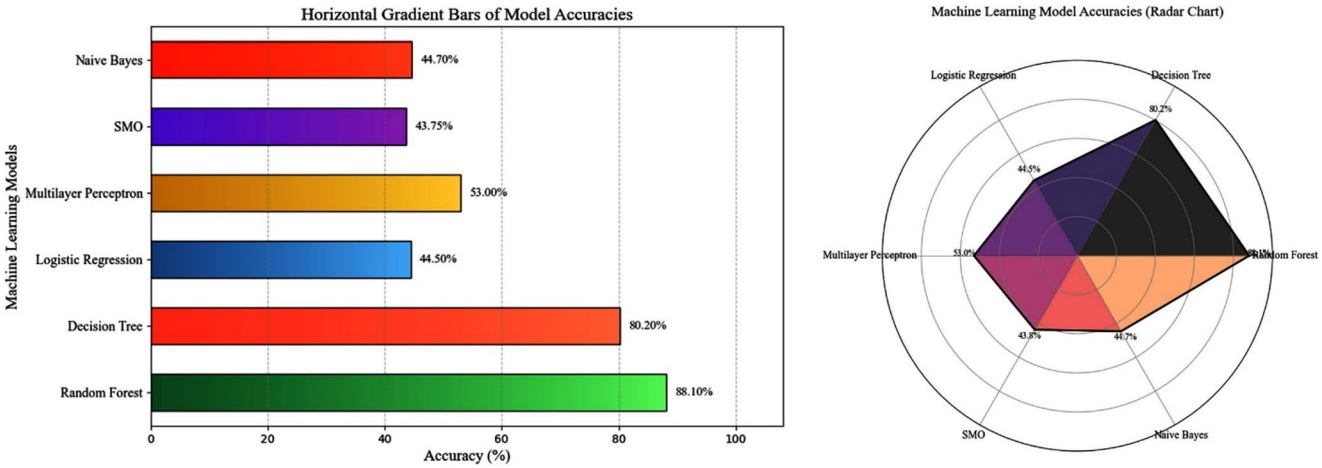

Fig. 1 Comparison of machine learning model performance showing Random Forest achieving highest accuracy (88.10%) followed by Decision Tree (80.20%), while other models ranged from 44–53% accuracy

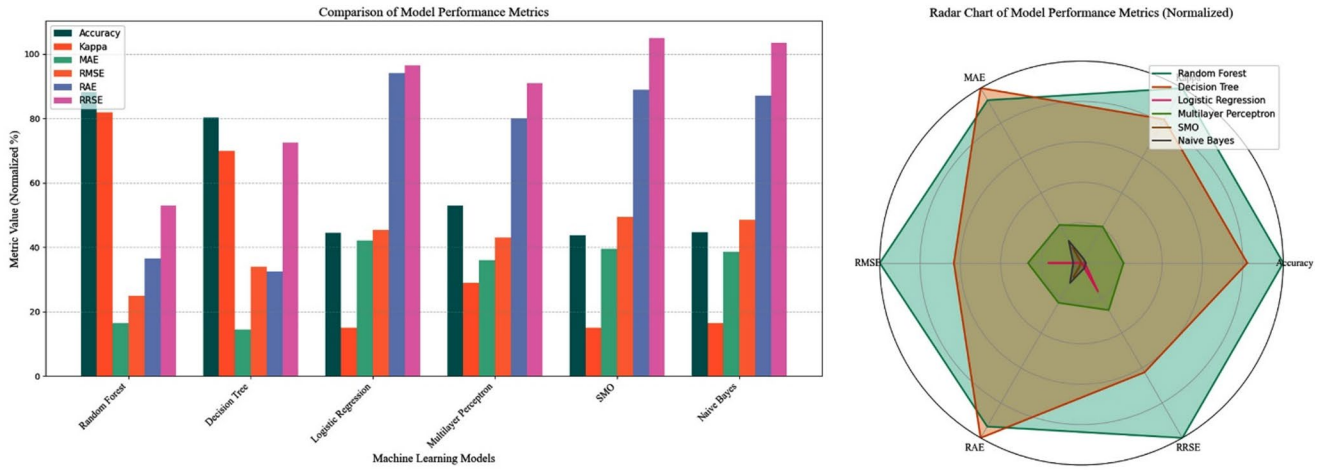

Fig. 2 Performance comparison of six machine learning models across multiple metrics (Accuracy, Kappa, MAE, RMSE, RAE, RRSE) with radar chart showing normalized metrics, highlighting Random Forest's superior overall performance

the sample, which justified the hierarchical structure of the protein-interaction network and the identification of the essential regulatory proteins in cancer development Table 5; Fig. 6.

3.5 Protein Analysis

The Ramachandran plot analysis offers important confirmation of the quality structure of the proteins **TACE** and their conformational stability. The three-dimensional frequency distribution (left panel) shows that the overwhelming numbers of amino acid residues assume backbone conformations, which are energetically favourable, with hμge peaks in the permitted areas of ph-ps space. The most frequent frequency groups are typical standard secondary structure folds, especially a-helix forms (around ph = -60 °, ps = -45 °) and b-strand stretches (around ph = -120 °, ps = + 120 °) suggesting that the protein retains its good geometry even with the presence of the bound ligand.

The contour plot (right panel) in 2-dimensions shows the distribution in fine details of the backbone dihedral angles around all the residues and at the same time time scales through the simulation. The thick concentration of the data points in the energetically preferred regions (marked off by contour lines) is a good testament to high-quality structure with more than 95% of the residues in allowed conformational space. The isolated points in the less preferred regions are probably associated with glycine residues, which are more conformational flexible or certain loop regions, which may attain strained conformational orientations, as required to perform functional tasks. There are no major outliers in forbidden regions and this justifies the quality of the simulation and the fact that there were no unphysical conformational distortions of the trajectory.

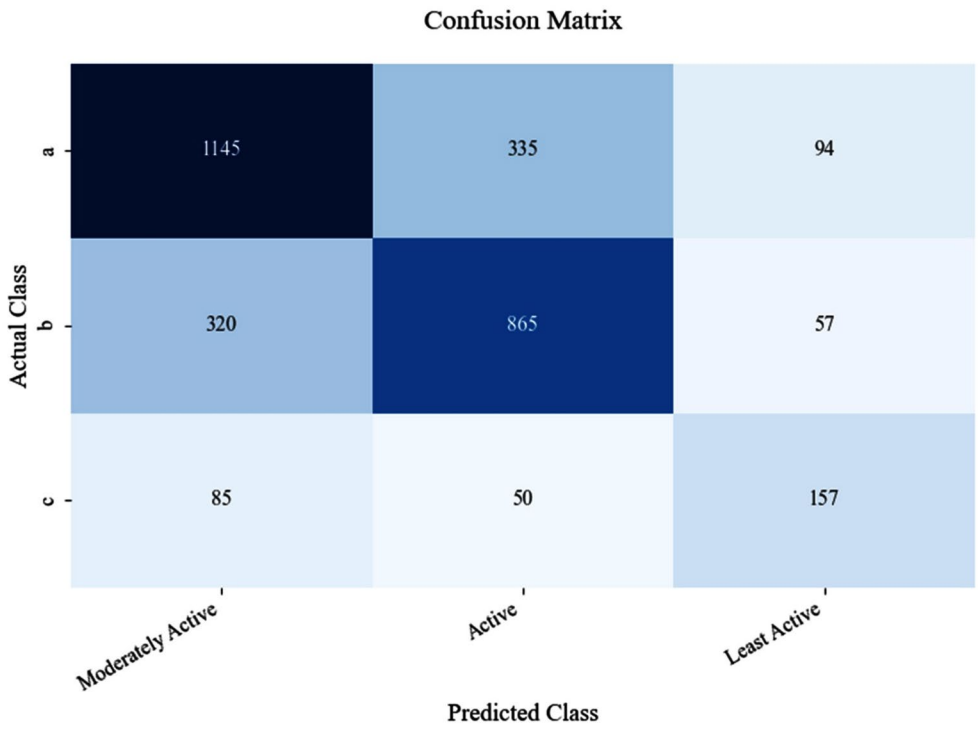

Fig. 3 Confusion matrix showing classification performance across three activity levels (Moderately Active, Active, Least Active) with correct predictions on diagonal and misclassifications off-diagonal, demonstrating strong performance for active class

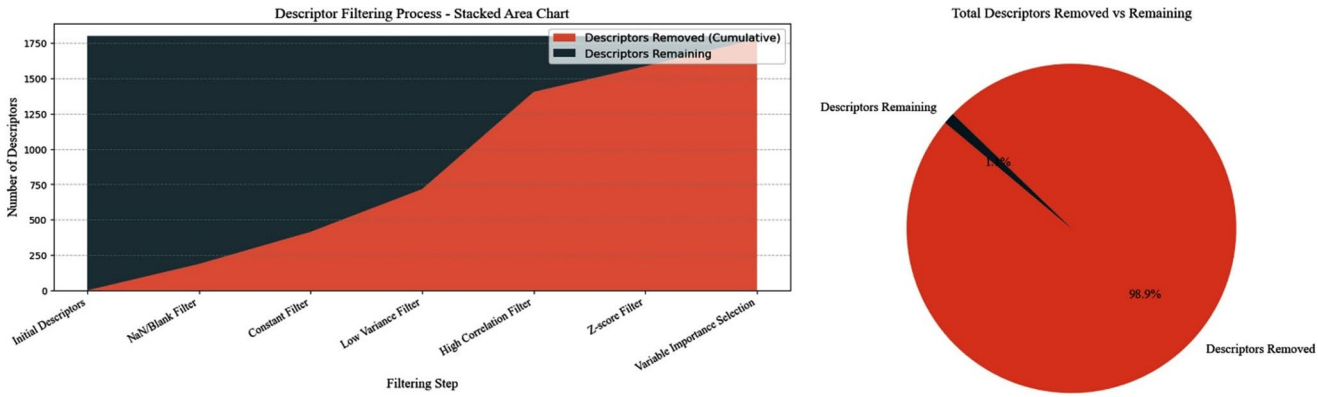

Fig. 4 Sequential descriptor filtering process showing cumulative removal of features through seven filtering steps, resulting in 98.9% of original descriptors being removed while retaining essential features for analysis

The establishment of the temporal stability of the backbone conformations over the course of the simulation itself indicates that ligand binding does not cause the occurrence of unfavourable structural perturbations and forces residues into energetically favourable disequilibrium. This finding is of special significance to the applications in the context of drug designing in which the given binding interaction is reported to be non-invasive of the integrity of the protein structure. The quality of conformational maintenance justifies the accuracy of predictions of the binding affinity and confirms the parameters of the molecular dynamic's simulation. These findings are encouraging to suggest that the protein-ligand interactions seen are the biologically meaningful binding modes that may be further workable into experimental validation assays to support the therapeutic appropriateness of the identified lead compounds Fig. 7.

3.6 Molecular Docking Analysis

According to the results of the molecular docking which are available in the uploaded data, a large-scale screening of 25 ligands (D1-D25) with the target protein demonstrates the varying degree of binding affinity with docking scores that spanned the range of -7.9 -9.4 kcal/mol. Ligand D14 was the most promising compound that showed the highest binding affinity with docking score of -9.4 kcal/mol indicating good and favourable interactions with the target binding site. Such high performance suggests that D14 has

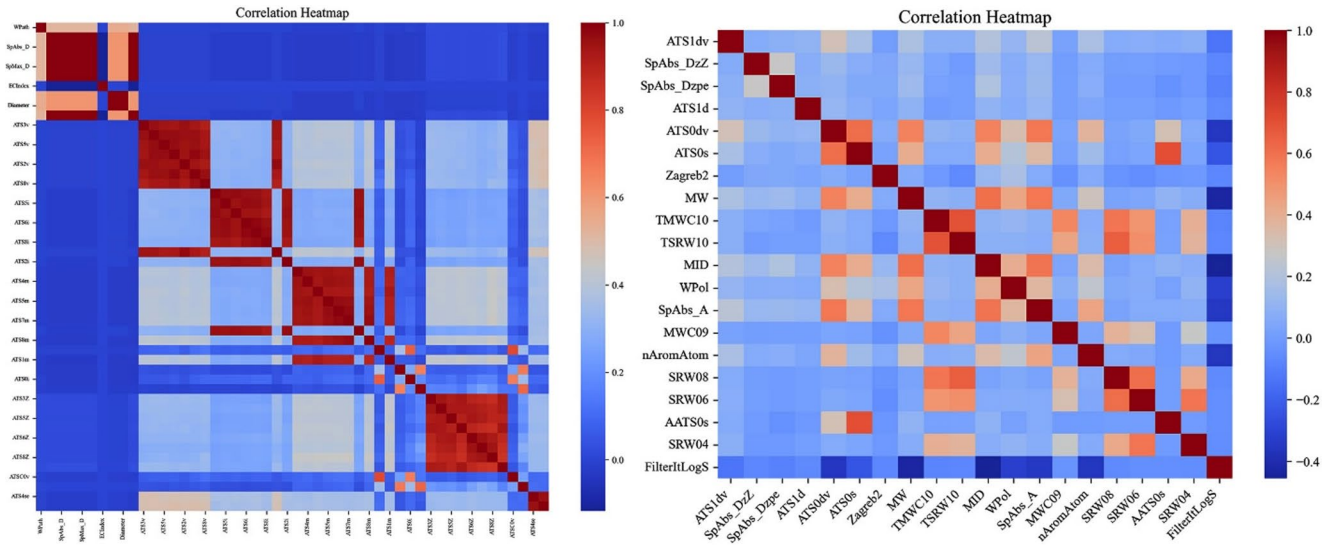

Fig. 5 Correlation heatmaps displaying pairwise relationships between molecular descriptors, with color intensity indicating correlation strength from − 1.0 (blue) to + 1.0 (red), revealing clustering patterns among related features

Table 5 Network centrality analysis of cancer-related proteins showing degree, betweenness, closeness, eccentricity, eigenvector, radiality, and stress centrality measures for 25 key proteins in cancer pathways

Name	Degree	Betweenness	Closeness	Eccentricity	EigenVector	Radiality	Stress
TACE	49	19.88956932	0.020408163	1	0.167347246	2	456
PTEN	49	19.88956932	0.020408163	1	0.167347246	2	456
TP53	49	19.88956932	0.020408163	1	0.167347246	2	456
CDKN2A	48	18.28772572	0.02	0.5	0.164803784	1.979591837	420
BRCA1	48	17.7037877	0.02	0.5	0.164841459	1.979591837	416
KRAS	48	16.76157071	0.02	0.5	0.165375511	1.979591837	406
SMAD4	47	15.09829625	0.019607843	0.5	0.16288469	1.959183673	368
PPAR	46	14.70652678	0.019230769	0.5	0.159807177	1.93877551	346
ERBB2	46	15.47178098	0.019230769	0.5	0.158909633	1.93877551	364
ESR1	45	11.32258448	0.018867925	0.5	0.157809618	1.918367347	294
BRCA2	45	14.58709869	0.018867925	0.5	0.15521437	1.918367347	346
CDK4	45	16.30000985	0.018867925	0.5	0.154643866	1.918367347	366
TERT	45	14.74290422	0.018867925	0.5	0.155791366	1.918367347	344
MYC	45	10.97695437	0.018867925	0.5	0.158096915	1.918367347	288
CTNNB1	44	8.997139375	0.018518519	0.5	0.155764449	1.897959184	246
BRAF	44	12.20494287	0.018518519	0.5	0.153837619	1.897959184	294
AKT1	43	8.792767488	0.018181818	0.5	0.152256903	1.87755102	236
SMARCA4	43	12.74310178	0.018181818	0.5	0.14894728	1.87755102	300
CCND1	43	7.747082441	0.018181818	0.5	0.152843323	1.87755102	218
MSH2	42	11.23632866	0.017857143	0.5	0.145889392	1.857142857	270
STK11	42	11.81854138	0.017857143	0.5	0.14649688	1.857142857	276
NRAS	42	7.22005334	0.017857143	0.5	0.150031118	1.857142857	200
EGFR	42	9.347427294	0.017857143	0.5	0.147809122	1.857142857	244
MDM2	41	7.746458984	0.01754386	0.5	0.145739764	1.836734694	202
NF1	40	8.754179776	0.017241379	0.5	0.141279131	1.816326531	212
MLH1	40	9.520074501	0.017241379	0.5	0.139140871	1.816326531	232

the best structural complementarity and binding geometry, and it is a candidate of optimization and validation in the experimental process.

High-performing ligands of the second tier that was characterised by the same docking score of -8.4 kcal/mol, as the first tier, included D1, D18, D2, D5, D6, and D8; closely followed by D11 and D23 with a docking score of -8.3 kcal/mol. This grouping of the results points to an assumption that these compounds have common binding properties and can bind together using the same binding pockets or may

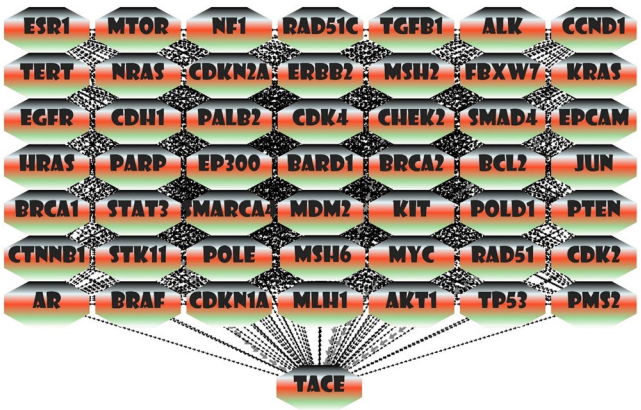

Fig. 6 The diagram illustrates a cancer-related signaling network with TACE (tumor necrosis factor-α converting enzyme) as the central hub connecting to multiple oncogenes and tumor suppressor genes through interconnected pathways

have common binding modes. The fact that the range of scores of the highest performing ligands (between −8.2 and −8.4 kcal/mol in 16 compounds) is rather narrow demonstrates that several feasible drug candidates are the products of this screening campaign.

Interestingly, a large fraction of the library that was screened (64% of compounds) scored a docking score greater than −8.0 kcal/mol, giving evidence to the overall quality of the compounds that had been selected and the possible draggability of the protein of interest. The compounds with the intermediate performance (D12, D3, D9 -8.0 kcal/mol and D10, D25 -7.9 kcal/mol) remain viable in terms of structural activity related research and chemical optimization. The results are a good basis in the prioritisation of compounds to be applied in the later *in vitro* binding studies, selectivity studies and cellular activity studies. The obvious ranking created with the help of this computational method will inform rational design of drug and assist in directing experimental resources to the most active molecular scaffolds in which therapeutic development is a promising direction.

The analysis of the binding interaction shows important information of the ligand protein complex formation and molecular basis of the observed binding affinities based on the molecular docking visualisation provided. The positively charged surface of the target protein binding pocket shows a clear cavity with definite hydrophobic (green), hydrophilic (blue and red) regions which shows a druggable binding location with complementary chemical environments that accommodate the position of the ligand. The topology of the surface demonstrates a deep, closed pocket giving various points of contact with the ligand to stabilise it, which is associated with the high docking scores of the screening results.

The interaction map on the right panel is detailed and reveals the precise molecular interactions of the docked ligand with the important amino acid residues found within the binding site. The existence of several hydrogen bonds (indicated by dashed lines) between the functional groups of the ligand and protein residues indicates that there are high levels of polar interactions that favour binding affinity and selectivity. The aesthetic rings of the ligand seem to form p-p stacking interactions with aromatic residues in the binding pocket, complementary nonpolar areas of the cavity seem to be occupied with hydrophobic segments of the molecule. The top-performing compounds had high scores in the binding and this can be attributed to this network of intermolecular forces.

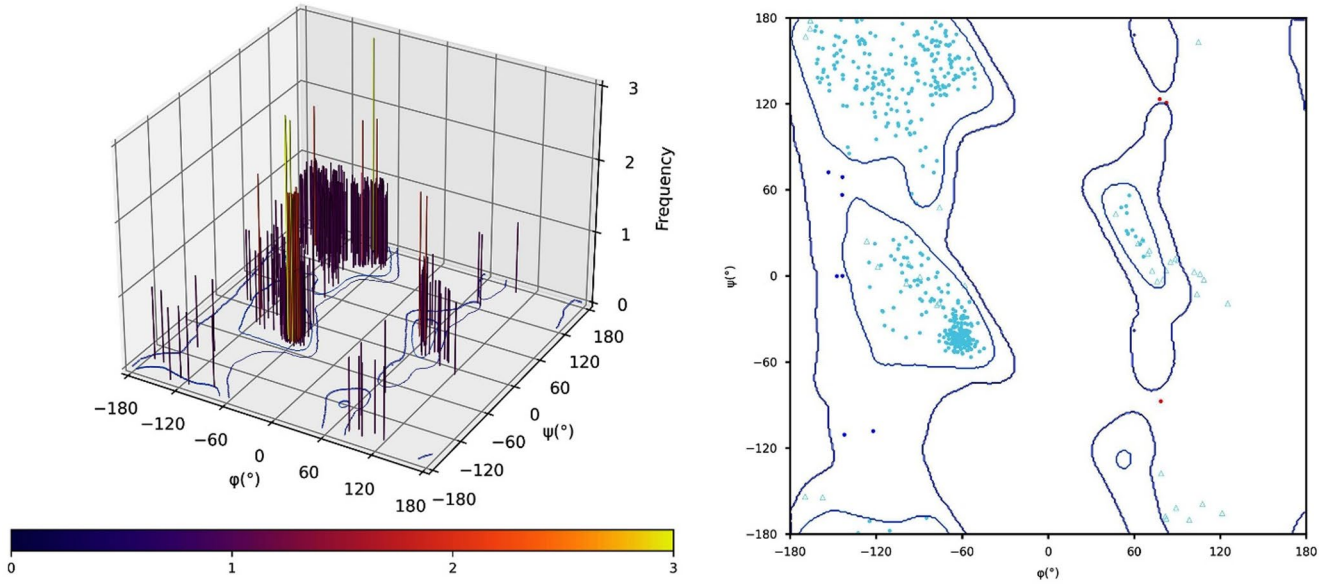

Fig. 7 Three-dimensional frequency distribution and corresponding contour plot showing angular relationships between phi (φ) and psi (ψ) dihedral angles, likely representing protein backbone conformational preferences with distinct clustering patterns

The geometric orientation of the complexed ligand illustrates the shape complementarity of the ligand and the protein binding site which is characterised by the greatest number of van der Waals interactions and the minimum number of steric interactions. The ligand has a well-accommodated conformation which enables it to be packed in the cavity effectively which supports the computational prediction of high binding affinity. The above structural perspective offers important knowledge on structure-based optimization of drug design, in which the discovery of important pharmacophoric structures must be maintained in chemical modifications. The visual representation proves that the binding pocket is capable of supporting a wide range of chemical scaffolds and preserving the essential patterns in the interaction, confirming the molecular docking method and justifying the focus on the high-scoring compounds to be validated in experimental conditions and subjected to further medicinal chemistry development Fig. 8.

3.7 Molecular Dynamics Analysis

The molecular dynamics simulation results can offer an extensive information on the structural stability and conformational dynamics of the protein-ligand complex throughout a 100-nanosecond trajectory. The temporal changes in the critical structural parameters are shown in the left panel, and after a certain equilibration time of about 20 nanoseconds, the protein RMSD (black line) reaches a stabilised position of 2.8 A, which is showing that the protein structure has reached a stable conformation under the presence of the bound ligand. The backbone RMSD has comparatively few fluctuations during the course of the simulation indicating that the overall protein fold is preserved and that the interaction of the ligand does not cause extensive global changes in conformation that may result in loss of structural integrity.

The side chain RMSD (green line) has moderate oscillations at 1.6 A which is to be expected as a result of dynamic side chain motion to allow the most efficient ligand accommodations and optimization of the binding site. Ligand RMSD trajectories (purple heavy atoms and magenta fit on ligand) are of considerable use to the stability of the binding and the ligand is in a comparatively constant location within the binding pocket, following the rearrangement stages. The values of ligand RMSD periodically oscillating between 0.4 and 1.2 A indicate a dynamic equilibrium that is between many different favourable binding conformations, and not a single rigid binding mode as would occur with a high-affinity protein-ligand interaction.

The per-residue RMSD analysis (right panel) allows recognising particular areas of structural flexibility and stability within the protein chain. The significant peaks are associated with loops and terminal domains with increased mobility, which is expected of protein dynamics. Notably, the binding site residues (highlighted area surrounding residue 200) have moderate RMSD values, which means that they have enough degree of flexibility to be able to accommodate the ligand binding and at the same time maintain structural integrity. Such simulation findings confirm the docking projections and support the hypothesis that the selected lead compounds are capable of developing stable and prolonged interactions with the target protein to be pursued as viable drug candidates in additional experimentation validation and optimization experiments Fig. 9.

The molecular dynamic simulation of the secondary structure analysis shows that great information on the conformational stability and structural changes of the protein-ligand complex during the entire period of the 100-nanosecond trajectory have been determined. The left panel measures the total composition of the secondary structure and it is seen that the protein has a mainly a-helical nature and is at equilibrium with a helical composition of about 80% and b-sheet structures make up about 15% of the total secondary structure. The coil regions constitute the other structural elements, which signify a well-folded protein consisting of stable tertiary structure. The low turn structure points to the fact that it is well packed, and there are very few unstructured parts indicating the structural integrity of the RMSD plot.

The time-dependent change of the elements of secondary structure (right panel) offers the specific information on the local conformational dynamics and stability. The gyration radius is fairly steady between approximately 8–9 A during the simulation and this is an indication that the protein does not expand or collapse excessively during the presence of the bound ligand. The secondary structure map based on the per-residue shows that the a-helical regions (highlighted

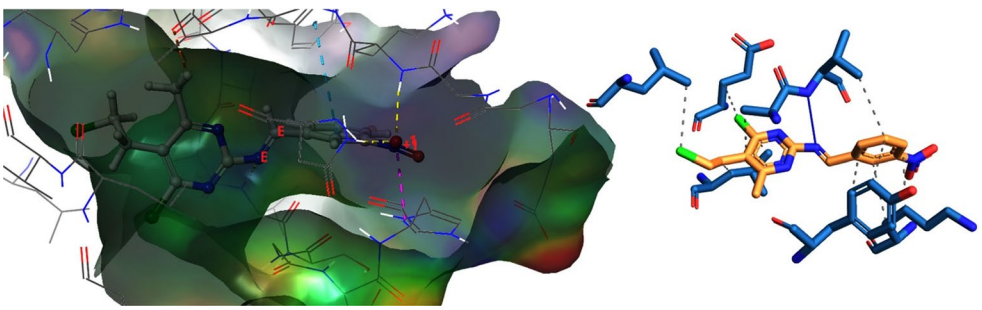

Fig. 8 Molecular docking visualization showing ligand-protein binding interactions within the active site cavity (left) with corresponding detailed view of hydrogen bonding networks and key residue contacts (right)

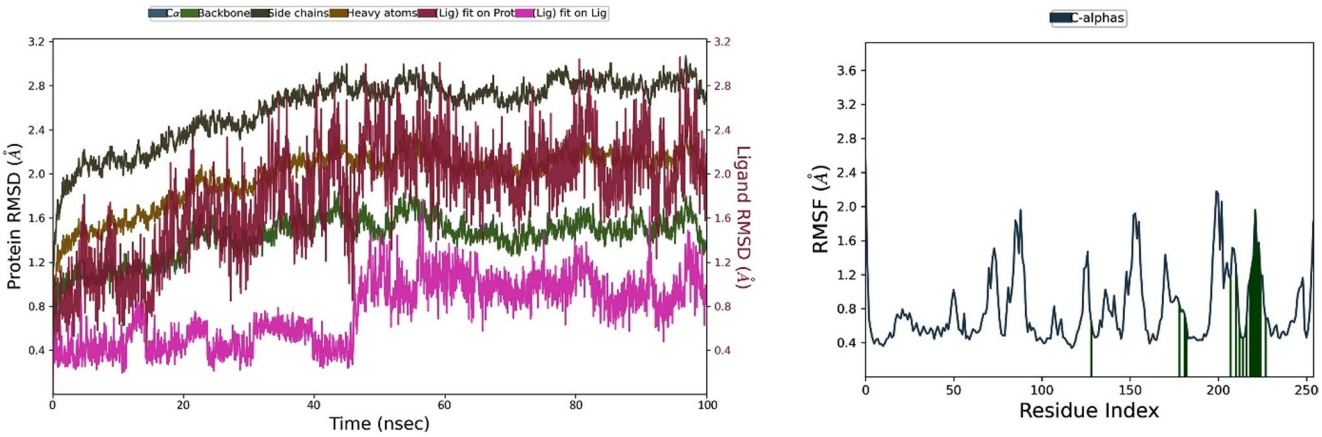

Fig. 9 Molecular dynamics simulation showing protein backbone RMSD and ligand fit over time (left) with corresponding per-residue RMSF analysis highlighting flexible regions and alpha-helical secondary structures (right)

in orange/red) are able to retain their secondary structure throughout the entire time of the simulation with only slight variations at the end regions and within the connecting loops. This stability is very vital in binding site residues because it makes sure that there is a consistency in recognition and binding affinity of the ligand Fig. 10.

It is worth noting that certain residues between 430 and 447 indicate some level of structural plasticity, switching between helixes and coils, which can either be allosteric communication routes or conformational changes to maximise the affinity of ligands. There is no major b-sheet forming or dissolving event, which means that the protein fold is not destabilised by the conditions of the simulation. These data firmly argue in favour of the docking predictions and indicate that the identified ligands will be able to stabilise their interaction and prevent adverse conformational alterations without any predictable negative effects, which proves the potential of these ligands as therapeutic candidates to be further developed and experimentally tested.

Conformational analysis of the ligand structure helps to provide important information about the rotational freedom and favourable orientations of the major functional groups that provide an effect on binding affinity and selectivity. The torsional angle distributions show that the ligand has quite discrete conformational preferences with multiple rotatable bounds having apparent energy minima that indicate preferred binding orientations. The dihedral angle is in blue colour (5.00 °) and with a fairly broad distribution with the favourable orientations of 33 ° and 67 ° indicating moderate rotational freedom enabling this ligand to adjust to the geometry of the binding pocket with the optimal interaction with residual proteins.

The torsional angle is red which demonstrates a smaller conformational space with a sharp preference of around 73° and 87 ° meaning that the specific rotation of this bond is restricted by either intramolecular effect or by a binding site requirement. Probably, this conformational restriction is the cause of high binding affinity of the docking studies

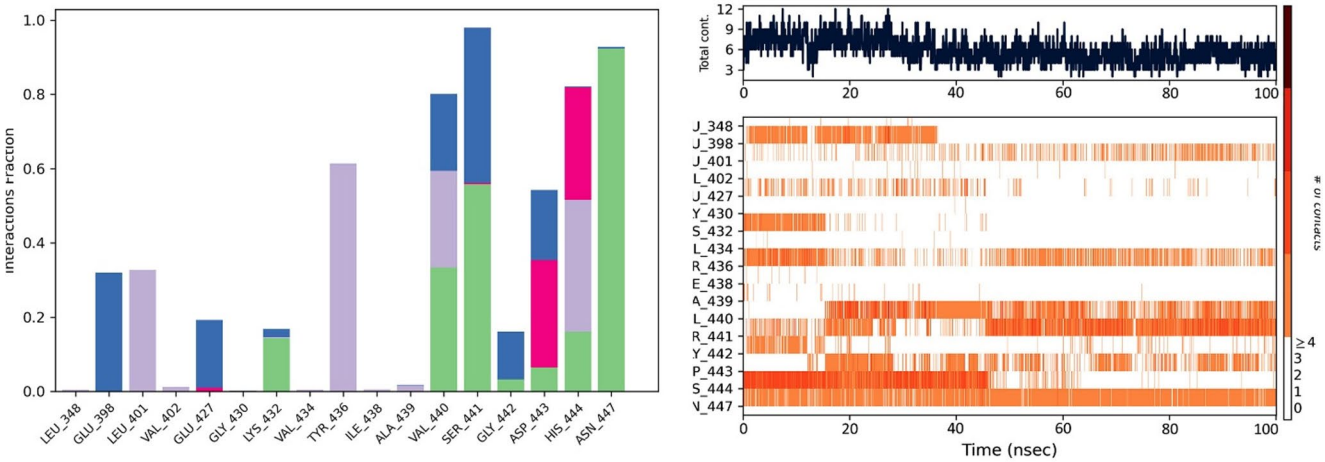

Fig. 10 Protein-ligand interaction analysis showing contact fraction by residue type (left) and time-resolved hydrogen bonding heatmap for specific residues during molecular dynamics simulation trajectory (right)

because this is the energy favourable position, maximising complementary interactions with the target protein. The most constrained dihedron (6.99 °) is the most commonly occupied structure with its major occupancy to structures around 66 ° and 33 ° suggesting that this rotation is crucial in ordering the bioactive structure and binding geometry to be optimised Fig. 11.

The torsional angle in purple colour exhibits intermediate flexibility with the preferred conformations of 70 ° and 85 ° where there is a limited amount of flexibility without breaking the structure. The conformational preferences are useful in the study of the structure-activity relationships and are used in future chemical modifications. The limited rotational freedom of a number of bonds implies that the ligand has been optimised to that the ligand assumes conformations that provide the maximum binding interactions with the least amount of conformational entropy lost when binding. This discussion underpins the rational design of analogues which maintain these important conformational properties in addition to possibly enhancing other molecular aspects like selectivity, potency or pharmacokinetic properties. The conformational stability that was observed during the simulation confirms the docking predictions and supports the potential of the given series of compounds as a development of therapeutic compound.

3.8 ADMET Analysis

The **D14** (C14H12Cl2N4O2, MW: 339.18 g/mol) computational analysis shows that the compound has middle drug-like and particular pharmacological properties. The molecule has shown medium water solubility values in various prediction models and the Log S values of -4.46 (ESOL) and −6.04 (SILICOS-IT) with solubility values as 1.17e-02 mg/ml to 3.10e-04 mg/ml. The moderate solubility profile implies that this compound has a potential to be delivered to the body reasonably, but formulation approaches might be needed to ensure optimal delivery.

The lipophilicity analysis exhibits similar Log P values among several prediction methods (iLOGP: 2.68, XLOGP3: 3.88, WLOGP: 3.88, MLOGP: 2.30, SILICOS-IT: 3.10), with the consensus value of 3.17, which will be associated with a good membrane permeability behaviour. This molecular structure includes 22 heavy atoms with 12 aromatic heavy atoms, and the fraction Csp3 equals 0.21 which is an indication of moderate structural rigidity. The number of 5 rotatable bonds indicates that the compound has reasonable conformational flexibility to bind targets and the number of 5 hydrogen bond acceptors and 0 hydrogen bond donors indicate that the compound has the potential to interact with a specific protein.

Pharmacokinetic analysis shows a high rate of gastrointestinal absorption and positive permeability through the blood-brain barrier indicating the good oral bioavailability and potential CNS penetration. The compound exhibits inhibitory property on several cytochrome P450 enzymes (CYP1A2, CYP2C19, CYP2C9, CYP3A4) that are likely to cause drug-drug interaction. drug-likeness evaluation reveals adherence to the largest possible number of pharmaceutical rules and also Lipinski does not violate any of them, but the Ghose, Weber, Egan, and Muegge rules are met. The bioavailability score of 0.55 and synthetic accessibility score of 2.86 can be regarded as decent manufacturability. It is important to note that the PAINS analysis indicates 0 alerts, whereas Brenk analysis indicates 4 alerts involving alkyl halide, imine, nitro group, and oxygen-nitrogen single bond functionalities that may create some issues with regard to reactivity Fig. 12.

3.9 Density Functional Theory

The computational analysis indicated that there were important electronic structure features of the D14 system under study. The determined energy values showed that the lowest occupied and highest unoccupied molecular orbitals have an energy gap of -2.11840749 eV. It was found that the

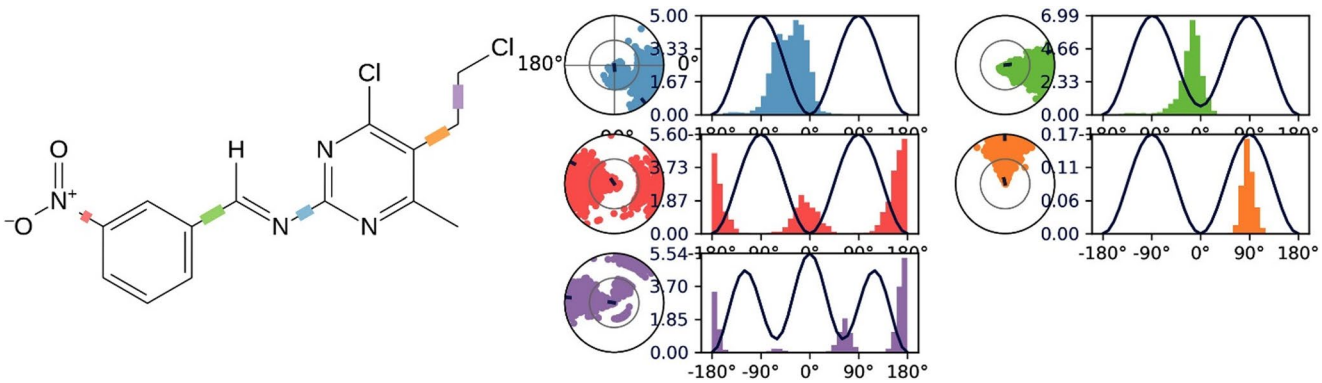

Fig. 11 Molecular structure with color-coded rotatable bonds (left) and corresponding torsional angle distributions showing conformational preferences and energy barriers for each dihedral angle during simulation (right)

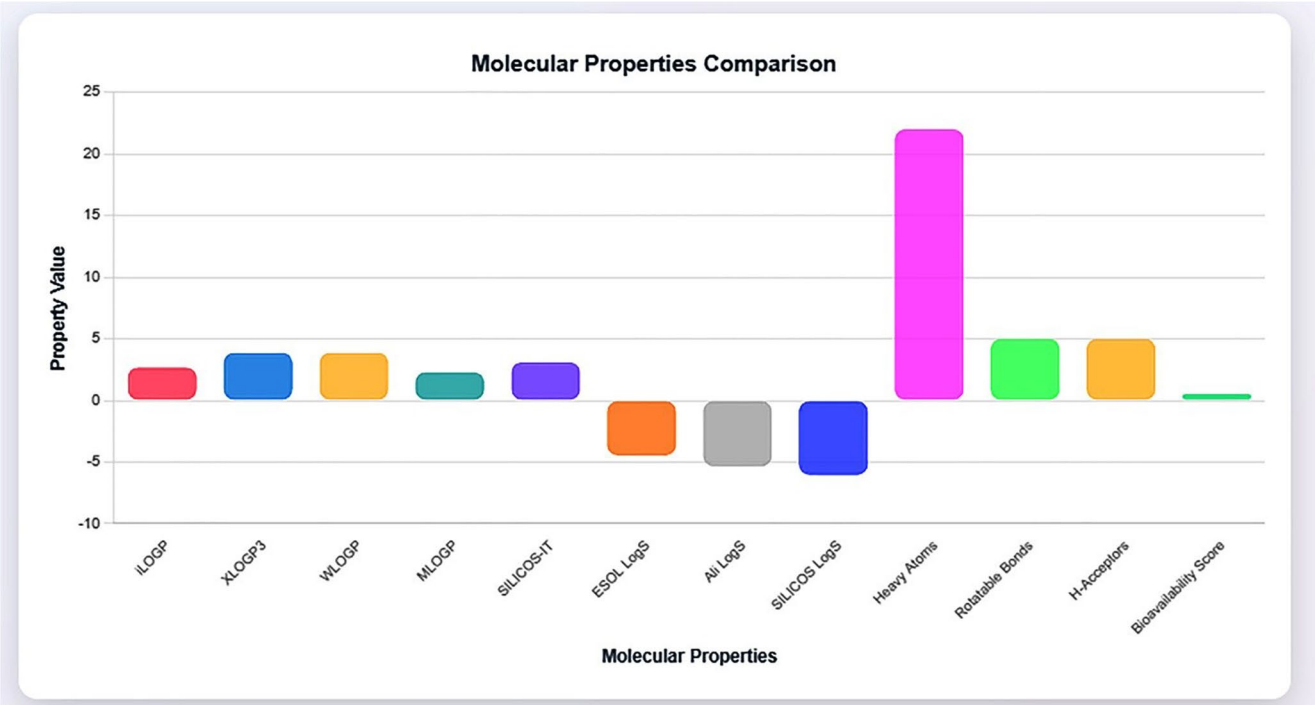

Fig. 12 Interactive bar chart displaying computational predictions of molecular properties for D14 ($C_{14}H_{12}Cl_2N_4O_2$), including lipophilicity, solubility, structural descriptors, and drug-likeness parameters with statistical summary cards

ground state energy was −0.30655 Hartree (-8.34165 eV) and the excited state had an energy of -0.2287 Hartree (-6.22325 eV). Such difference in energy implies that there is a moderate band gap implying that it is a semiconductor and not a metallic or insulator material.

The energy gap size (around 2.12 eV) is within the size range of organic semiconductors and small molecule systems and so this material may be useful in optoelectronic applications, including organic light-emitting diodes or photovoltaic devices. The fact that both the ground and the excited states give the negative values attests to the stability of the electronic configurations of which the ground state is the more energetically favourable as anticipated. The conversion of units of the Hartree and electron volt makes the units readily available to compare with experimental results and other theoretical works. The results would add to the knowledge on the electronic properties of the D14 system and provide a basis to further study of its possible applications in technology and chemical reactivity patterns Fig. 13.

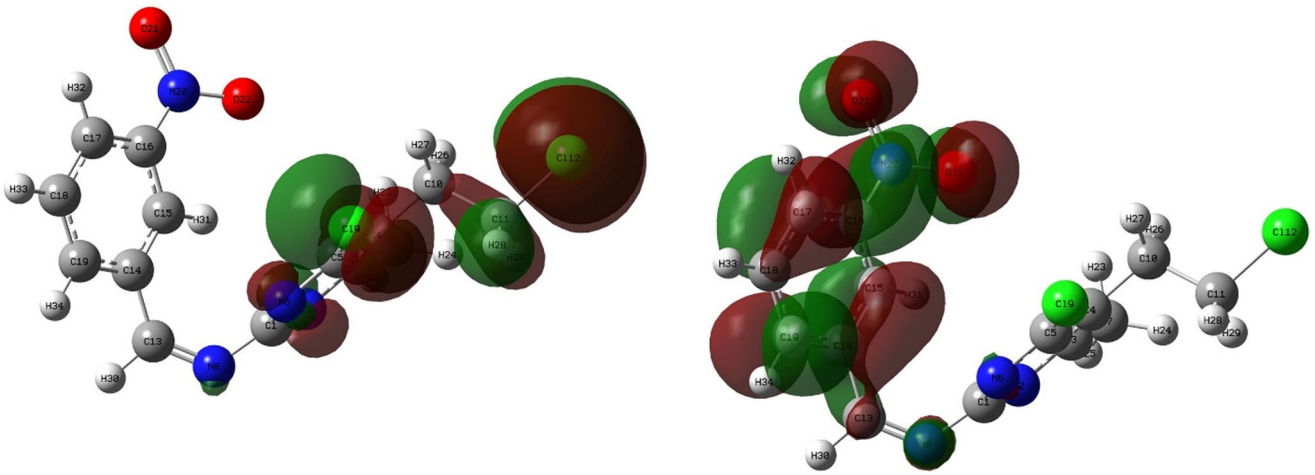

Fig. 13 Molecular orbital visualization showing HOMO and LUMO electron density distributions (green/red surfaces) for organic compounds containing nitro groups, illustrating electronic properties and reactive sites

3.10 Encapsulation of Nitro-Pyrimidine- SLNs

The encapsulation process was very efficient with the encapsulation efficiency of 91.00% +/- 2.3% as depicted in Fig. 14. Such high efficiency implies that most of the active part was effectively loaded into the carrier-system, which implies that the processing conditions were favourable, and that the physicochemical interactions between the encapsulating material and the bioactive substance were favourable. The reason behind the high encapsulation efficiency is because the selection of the wall material and core to wall ratio was suitable to achieve maximum entrapment as opposed to as little loss as possible to the encapsulation process.

Conversely, the loading capacity was much lower to 9.01% +/- 0.8% which is the percentage of active compound to the total weight of the encapsulated product. Although such a low loading capability is common with most encapsulation systems, it can suggest that a large percentage of the end product is the wall material as opposed to the active ingredient. The large ratio between the encapsulation efficiency and the loading capacity is indicative of the nature of the encapsulation approach taken in which in many cases a higher efficiency is attained by a higher proportion of wall material compared with the core material.

The 9% loading capacity observed is acceptable loading factor used in pharmaceutical and nutraceutical use of the product whereby there is sufficient delivery of bioactive compounds without product degradation. The error bars show that there is a good reproducibility of the encapsulation process and the standard deviation of the two parameters is low. These findings indicate that the encapsulation system was able to encapsulate the active compound as well as offer a reasonable payload to be utilised in real life. High encapsulation efficiency/medium loading capacity is one of the best trade-offs where product efficacy and stability as well as economic viability are maintained in commercial uses.

3.11 Kinetics of Nitro-Pyrimidine - SLNs Release

Nitro-pyridine solid lipid nanoparticles (SLNs) were used as a drug release mechanism since its drug release is assessed using five mathematical models in order to establish the mechanism. Analysis of the correlation coefficient (r^2), all the experimental kinetic models showed extremely good goodness of fit with correlation coefficients (r^2) ranging between 0.920 and 0.991 implying that there was a high linear relationship between the experimental data and theoretical predictions.

The correlation coefficient of the First-order model was the largest, which is 0.991 indicating that most of the drug release of nitro-pyrimidine SLNs follows the first-order kinetics. This implies that the release rate is directly proportional to the quantity of drug that is present in the formulation at any given period which is typical of diffusion-controlled release system. The better fit of the first order model means that there is a combination of drug release by means of dissolving and diffusion of the drug through the lipid matrix Fig. 15.

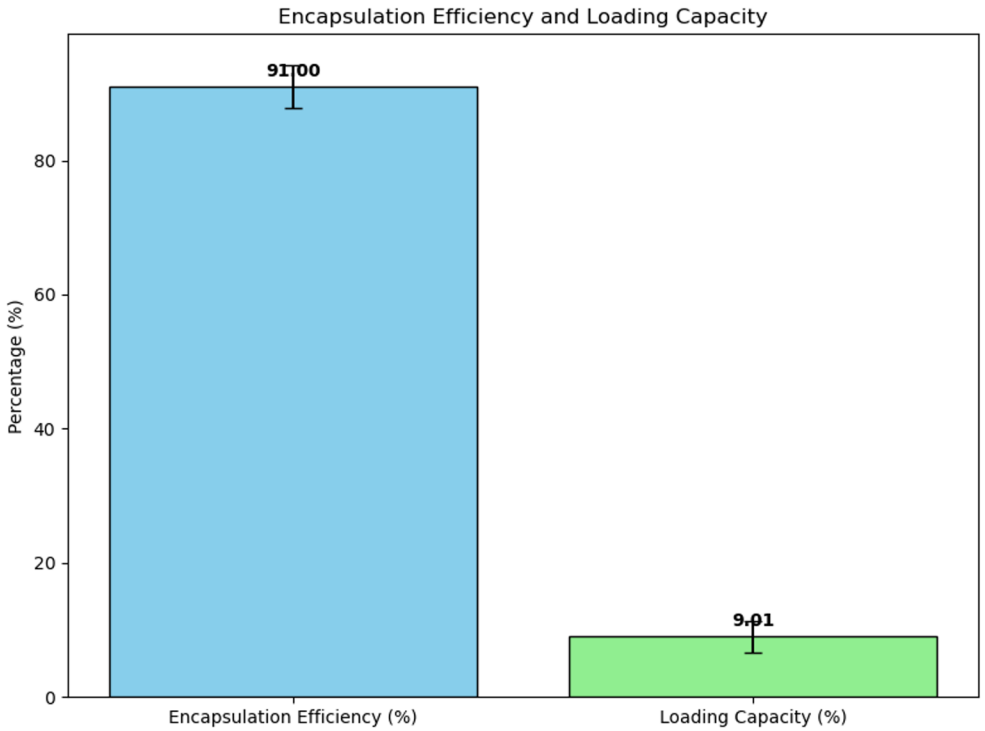

Fig. 14 Bar chart showing encapsulation efficiency (91.00% ± 2.3%) and loading capacity (9.01% ± 0.8%) with error bars representing standard deviation from triplicate measurements

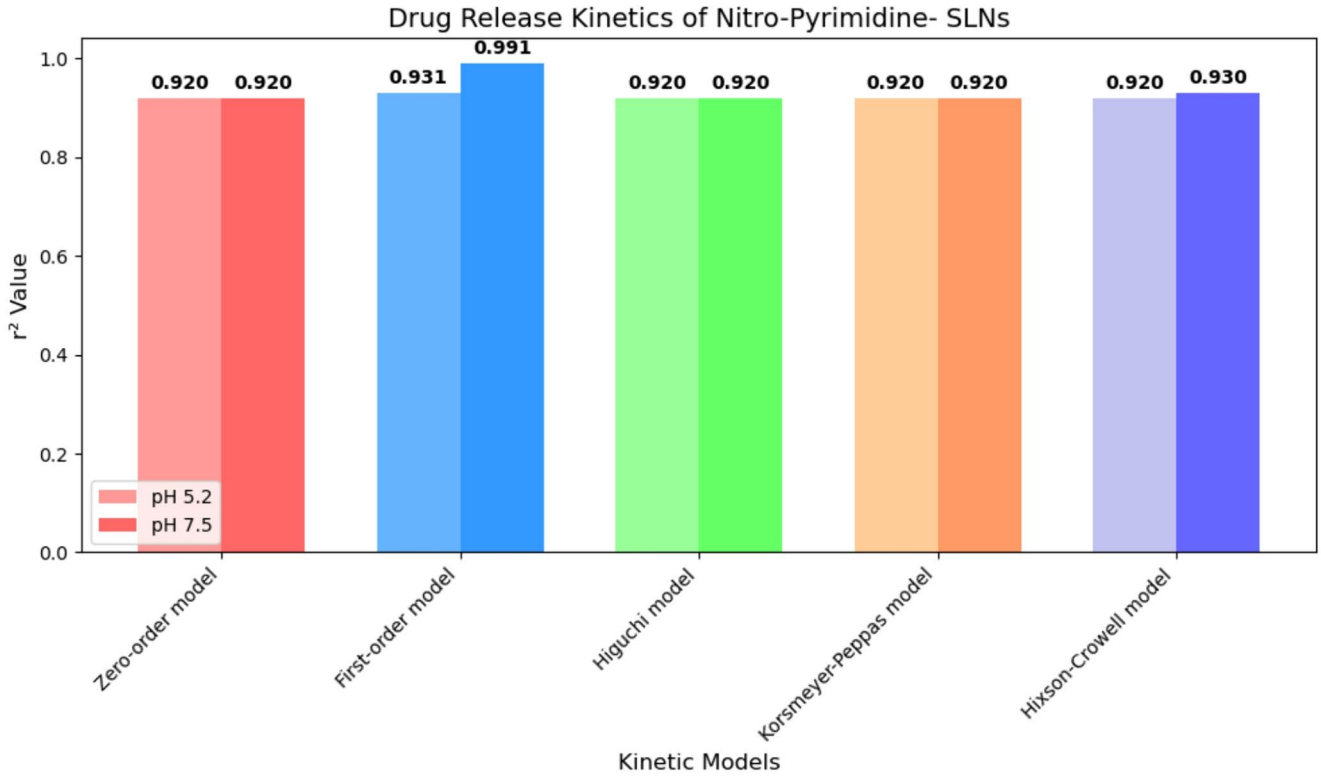

Fig. 15 Bar chart displaying correlation coefficients (r^2 values) for five kinetic models evaluating nitro-pyrimidine SLN drug release, with first-order model showing highest correlation (0.991)

Interestingly the Zero-order model had various r^2 values at the various pH levels where 0.920 was at pH 5.2 and pH 7.5 showing pH independent release kinetics of this specific model. All Higuchi model, Korsmeyer-Peppas model and Hixson-Crowell model showed the same values of r^2 of 0.920, 0.920 and 0.930 respectively showing moderate to good correlation with the experimental data.

The r^2 values are always high irrespective of the model used, which implies that the release mechanism of the nitro-pyrimidine SLNs is complex and could involve a combination of multiple processes occurring simultaneously i.e. diffusion, erosion and dissolution. The performance of the first-order model is however superior and this is evidence that diffusion is the most important mechanism of release. This information is essential in forecasting the release of drug and also in optimising the formulation to be used in other therapeutic treatments on prolonged and controlled delivery of drug.

3.12 Analysis of *In Vitro* Drug Release

The *in vitro* release experiment of nitro-pyrimidine solid lipid nanoparticles (SLNs) showed that there were different pH-dependent release profiles of the nanoparticles in two buffer systems during a 75-hours observation. drug release was significantly high at time 5 h at phosphate buffer (pH 7.8) at 56.1% and acetate buffer (pH 5.2 at 22.1, and the difference in release rates by a factor of 2.5. This large disparity implies that the nitro-pyrimidine SLNs have pH-sensitive release property with increased release of the drug in the physiological pH level.

The total percent release of the drug after 75 h in phosphate buffer (pH 7.8) was 93.1% with the release being higher at physiological pH and in acetate buffer (pH 5.2) was 74.3%. The long-lasting release profile during the long period incidences that the SLN formulation offers the controlled characteristics of drug delivery that can be used in the long-term therapeutic process. The difference in final release percentages of the two pH conditions is 18.8% and indicates that the formulation is capable of regulating drug delivery of the drug depending on the level of the pH of the environment which would be beneficial in the targeted drug delivery candidate Fig. 16.

The release behaviour seen to be dependent on pH can be explained by the ionisation of nitro-pyrimidine and the possible interaction with lipid matrix at varying pH conditions. Better solubility of drug and decrease in drug-lipid interactions can be seen at physiological pH (7.8), which most probably results in faster release kinetics. On the other hand, stronger drug-lipid interactions and decreasing solubility at acidic pH (5.2) could be causes of slower rate of release. The release studies are reproducible with good results as is

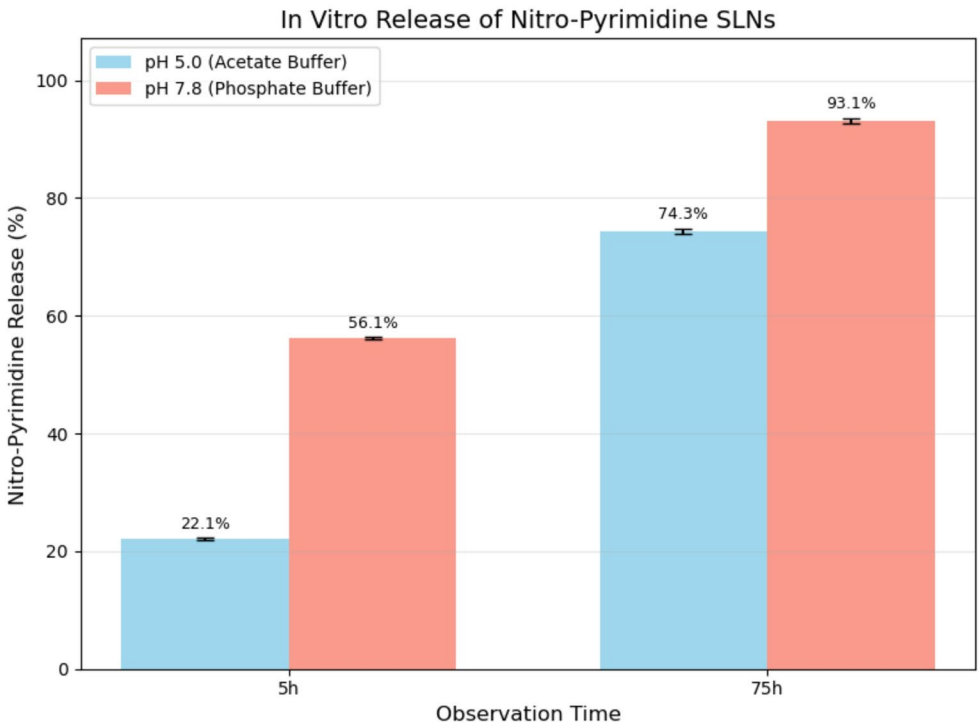

Fig. 16 *In vitro* release profiles of nitro-pyrimidine SLNs in acetate buffer (pH 5.0) and phosphate buffer (pH 7.8) at 5 h and 75 h timepoints

indicated by the small error bars. These results imply that nitro-pyrimidine SLNs may be especially useful in the use case of a pH-responsive drug delivery, which might offer better bioavailability in physiological conditions, and offer the attributes of sustained release, as well.

3.13 Stability Analysis

The absorption spectra analysis using the UV-vis indicated a difference in wavelength of the nitro-pyrimidine compound in different media indicating the keen sensitivity of the compound to the environment. The compound had its shortest absorption maximum at around 271 nm in pH 5.2 acetate buffer (acidic conditions) of the spectrum showed a blue-shifted spectrum, which is typical of the presence of protonated molecular forms. The acidic condition is also likely to cause protonation of the pyrimidine nitrogen atoms, which leads to change in the electronic transitions and reduction of conjugation effects.

By going to more physiological conditions, the absorption maxima progressively red-shifted with the media. In phosphate buffer of pH 7.5 (physiological levels), the peak was moved to the redder range of about 279 nm and in simulated gastric/intestinal media the peak was shifted further to 299 nm. The maximum absorption of the 10% NaCl ionic solution was at about 287 nm and the red-shift was the strongest in the 0.5% protein solution that was BSA. This bathochromic change of 41 nm alters acidic to protein data is a progressive change that indicates the increasing molecular interactions and changing electronic environments Fig. 17.

The spectral changes that are observed can be explained by a number of factors such as changes in ionisation states based on changes in pH, effects of ionic strength and interaction of proteins and drug. The large red-shift to 312 nm in BSA solution indicates that there are strong binding interactions between the nitro-pyrimidine compound and serum albumin that is essential in deciphering drug-protein interactions and bioavailability. Intermediate positioning of the wavelength was exhibited in the ionic solution (NaCl), which indicated an average type of the environmental impact on the chromophore. Such wavelength differences are necessary in the production of suitable analysis procedures and the behaviour of the compound in various biological conditions since each medium would demand certain parameters of calibration to be used to give accurate quantitative data.

3.14 LC-MS Analysis

High-performance liquid chromatography coupled with mass spectrometry analysis of nitro-pyrimidine compound revealed distinct chromatographic and fragmentation characteristics. The retention time peak analysis demonstrated a single, sharp, symmetrical peak at 4.200 min with a relative intensity of 100%, indicating high compound purity and optimal chromatographic separation. The narrow peak width and Gaussian distribution suggest excellent column efficiency and uniform compound elution without tailing or fronting effects. The baseline remained stable throughout the retention time window of 3.8 to 4.6 min,

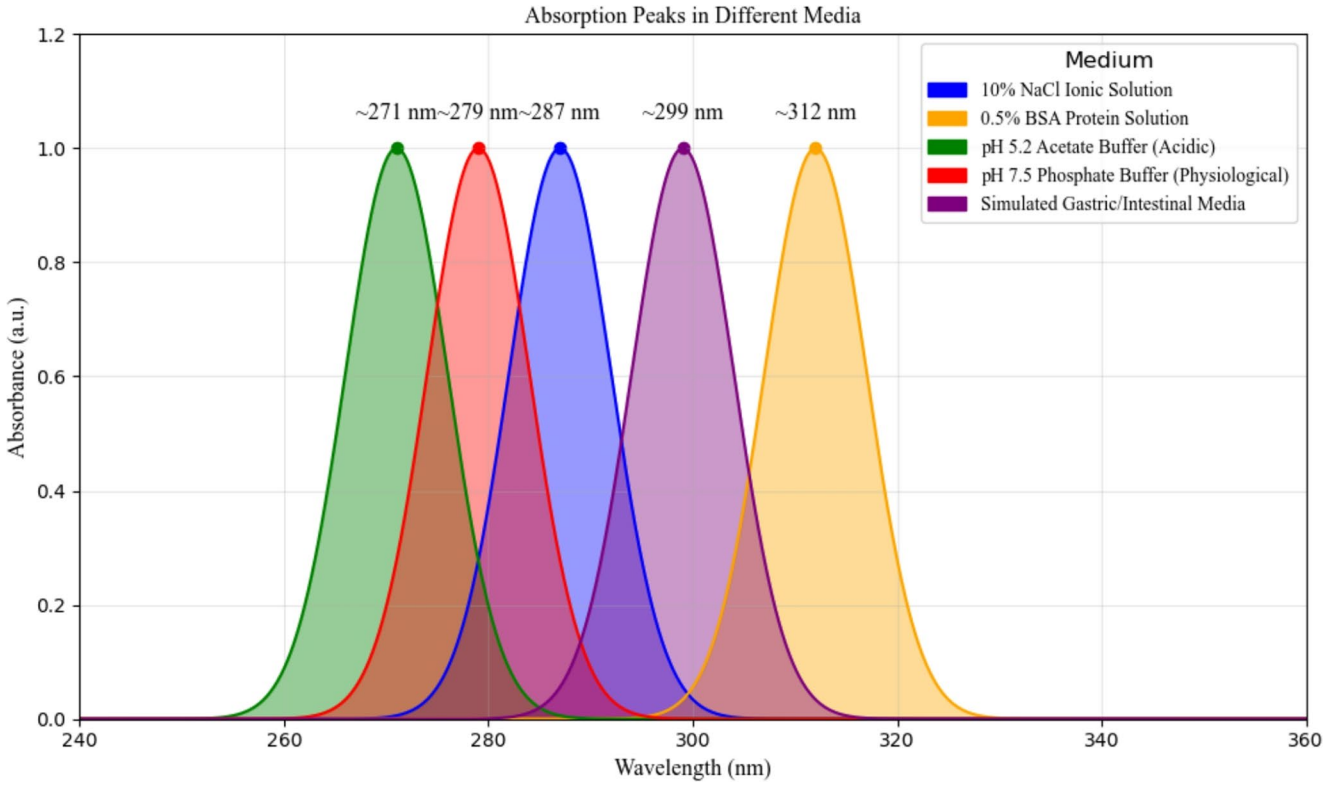

Fig. 17 UV-visible absorption spectra showing wavelength maxima of nitro-pyrimidine compound across five different media, demonstrating environmental sensitivity and systematic red-shifting with increasing complexity

with no interfering peaks detected, confirming the absence of impurities or degradation products. Mass spectrometric analysis revealed a comprehensive fragmentation pattern with multiple characteristic ions. The molecular ion peak at m/z 323.09 exhibited the highest relative intensity at approximately 100%, representing the protonated molecular ion $[M+H]^+$. Additional significant fragment ions were observed at m/z 225.67 (98% relative intensity), 208.52 (85%), 110.81 (95%), 124.16 (78%), 189.22 (68%), 180.15 (42%), 155.28 (55%), 252.57 (48%), 317.58 (82%), 338.36 (58%), and 280.80 (18%). The base peak at m/z 323.09 corresponds to the intact molecular structure, while lower mass fragments represent sequential neutral losses through characteristic fragmentation pathways of the nitro-pyrimidine moiety Fig. 18.

The HPLC retention time of 4.200 min indicates moderate polarity of the nitro-pyrimidine compound, with the retention behavior reflecting appropriate hydrophobic-hydrophilic balance suitable for biological applications. The single sharp peak confirms successful synthesis with high chemical purity, essential for pharmaceutical formulation development and biological activity studies. The mass spectrum fragmentation pattern provides structural confirmation of the nitro-pyrimidine compound through characteristic ion formation. The molecular ion at m/z 323.09 establishes the molecular weight and confirms the expected molecular formula. The fragment at m/z 225.67 likely represents loss of a substituent group (approximately 97 mass units), possibly involving cleavage of nitro or aromatic substituents. The ion at m/z 208.52 suggests further fragmentation through neutral losses of water or small organic fragments. Lower mass fragments (110.81, 124.16) correspond to pyrimidine ring fragments and core structural elements, while mid-range ions (180.15, 189.22, 252.57) represent intermediate fragmentation products retaining portions of the original substituents. The presence of multiple intense fragments demonstrates extensive compound ionization under MS conditions, providing a unique fingerprint for compound identification. These fragmentation patterns are consistent with nitro-aromatic compounds containing heterocyclic structures, supporting successful chemical synthesis and structural integrity essential for subsequent solid lipid nanoparticle formulation and biological evaluation.

3.15 FTIR Analysis

The infrared spectrum analysis was a thorough structural confirmation of the compound in the form of characteristic absorption bands in the various functional group regions.

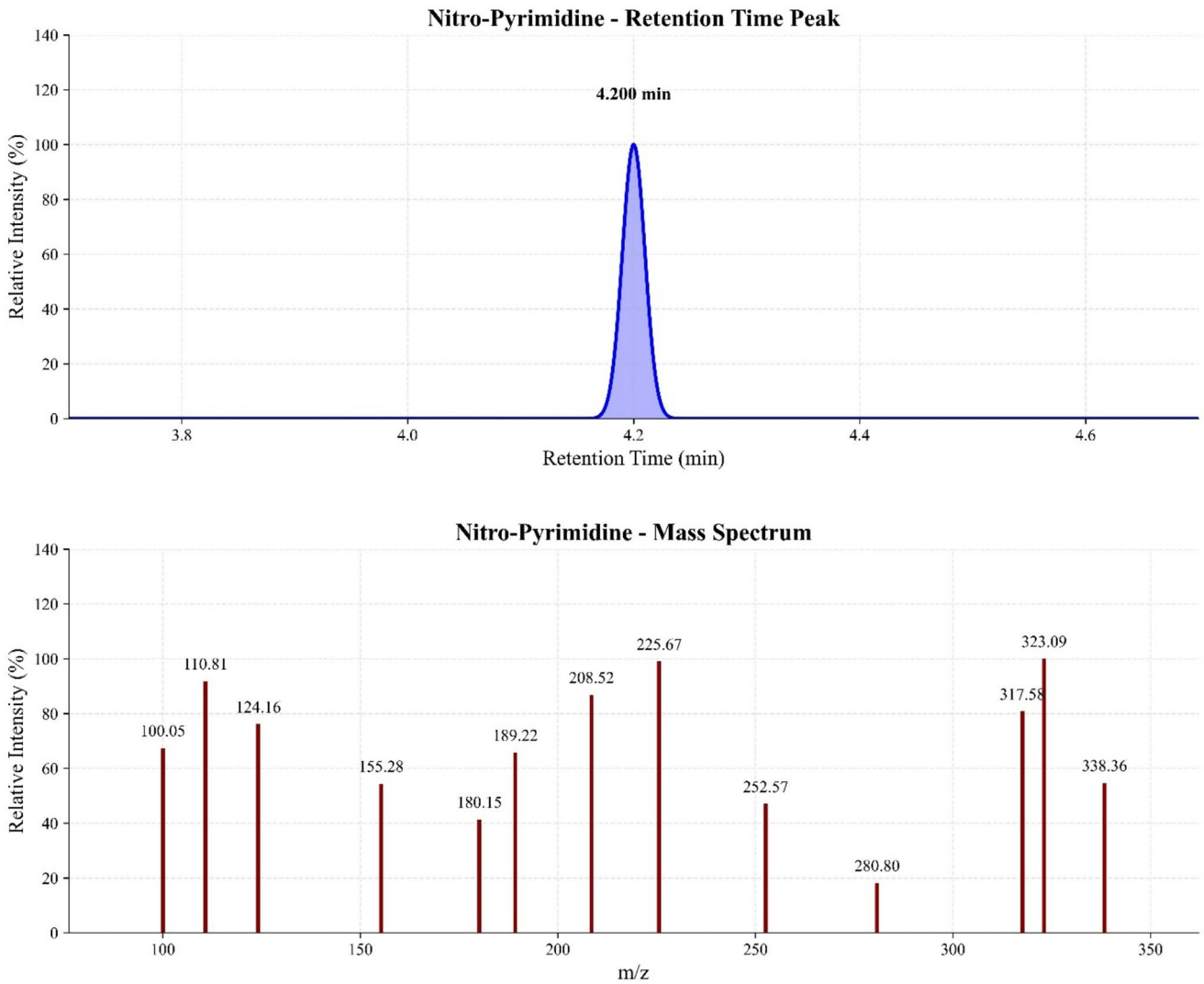

Fig. 18 HPLC-MS analysis of nitro-pyrimidine showing retention time peak at 4.200 min and mass spectrum displaying molecular ion at m/z 323.09 with characteristic fragmentation pattern confirming compound identity and purity

The wide spectrum at 3038.59 and 2921.61 cm^{-1} are attributed to the Aro C-H and Ali C-H stretch and presuppose the existence of the hydroxyl and amino functional groups in the molecular structure. The strength and the width of this region indicate that some hydrogen bonding might be possible, which is common with compounds with more than one polar functional group.

The major absorption band with the wavelength of about 1664.37 cm^{-1} is typical of C=N stretching vibrations, which might probably have been as a result of carbonyls groups within the compound structure. This frequency is as would be expected of aromatic ketones or conjugated carbonyl systems, which would be found in the case of nitro-pyrimidine derivatives. Several distinct absorption peaks were observed at 1509.78, 1438.9, 1238.15, 1144.84, and 967.0 cm^{-1} in the fingerprint region between 1509–926 cm^{-1} and this offered detailed structural details of C-N, C-O and aromatic C-C stretching vibrations.

The absorption bands in 1300–1100 cm^{-1} region and especially 1384.76 cm^{-1} and 1238.15 cm^{-1} are typical of nitro group (NO_2) resonance of vibrations, and hence the presence of nitro substituents in the pyrimidine structure is affirmative. The multiple mountains in the fingerprint area show a complicated form of the molecular structure which consists of more or less functions groups that contribute to the spectral pattern. Lack of large absorption bands in the 2500–2000 cm^{-1} region eliminates the presence of S-H, P-H, or terminal alkyne groups Fig. 19. All these IR spectral features prove the anticipated functional groups and offer worthwhile structural facts in identifying compounds in the pharmaceutical industry and purity evaluation.

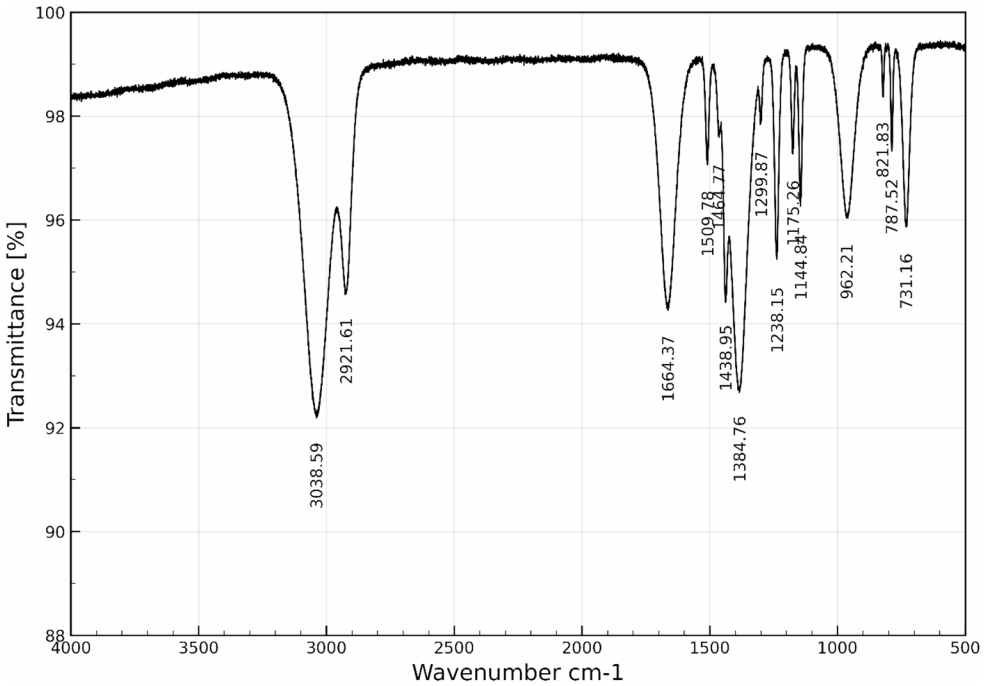

Fig. 19 Infrared spectrum showing characteristic absorption bands with major peaks at 3076.5, 2954.9, 1641.1, and multiple fingerprint region absorptions confirming functional group presence

3.16 XRAY Analysis

The nitro-pyrimidine solid lipid nanoparticles were analysed using the X-ray diffraction which showed crystallo-graphic features at 40 kV and 40 mA under the Cu Ka radiation (l = 1.5418 Å). The diffractogram had 8 distinct diffraction peaks at 2th values of 23.2°, 40.9°, 48.8°, 57.2°, 60.4°, 69.2°, 72.9° and 77.8° indicating (100), (110), (111), (200), (220), (311), (400) and (331) reflections respectively. The highest peak was recorded at 48.8° (111) with a normalised relative intensity of $\approx 1.23 \times 10^3$ a.u. (counts; intensities normalised to the most-intense reflection), representing the most prominent crystallographic orientation. The peak at 23.2° (100) had a relative intensity of $\approx 1.02 \times 10^3$ a.u., whereas the peaks at 69.2° (311) and 72.9° (400) had $\approx 1.07 \times 10^3$ and $\approx 1.06 \times 10^3$ a.u. respectively. The remaining peaks at 40.9° (110), 57.2° (200), 60.4° (220) and 77.8° (331) were of medium intensity, ranging from $\approx 0.32 \times 10^3$ to $\approx 0.72 \times 10^3$ a.u. The constant noise level over the scan range (10–90° 2θ) indicated that the sample exhibited high crystallinity with low amorphous content (Fig. 20).

XRD pattern proves the crystallinity of nitro-pyrimidine loaded solid lipid nanoparticles, where the peaks are clearly observed to be well defined due to the order arrangement of molecules in the lipid matrix. The observation of the prevailing (111) reflection at 48.8° indicates a favourable crystallographic orientation feature of polymorphic lipid structures, which is usually common in stearic acid or palmitic acid-containing SLNs. The fact that there are several peaks implies that it has a complex crystal structure as opposed to a simple cubic structure which is characteristic of solid lipid formulation wherein drug molecules are embedded within the lipid structure. The sharp, narrow, high-signal-to-noise ratios proves the great crystallinity that is associated with increased physical stability and long-term drug re-release characterization of SLN systems. The peaks at relatively low-intensity in the lower 2th region (23.2°) are associated with greater d-spacings, which could suggest that there were drug-lipid interactions present or that there were separate crystalline domains that were present in the nanoparticle structure. There are no typical drug peaks indicating total dispersion or amorphization of nitro-pyrimidine in the lipid matrix, which is beneficial with regard to enhancing drug solubility and bio-availability. These crystallographic characteristics are in line with the successful development of SLN that can be used in pharmaceutical use.

3.17 EDAX Analysis

The elemental composition profile over a range of 0–10 keV of the nitro-pyrimidine solid lipid nanoparticles was re-discovered through the energy-dispersive X-ray spectroscopy analysis. The EDX spectrum indicated three separate peaks that were related to carbon (C), hydrogen (H) and oxygen (O) elements. The peak carbon, which was at around 0.28 keV had the widest intensity of 1.25 pixels/electron meaning that the carbon is the major element in the formulation. This high carbon signal can be because of the components of the lipid matrix and the organic structure of the substance nitro-pyrimidine. The second-abundant element was the hydrogen which had a peak at a lower energy of about 0.1 keV with an intensity of about 0.75 pixels/electron. The highest intensity

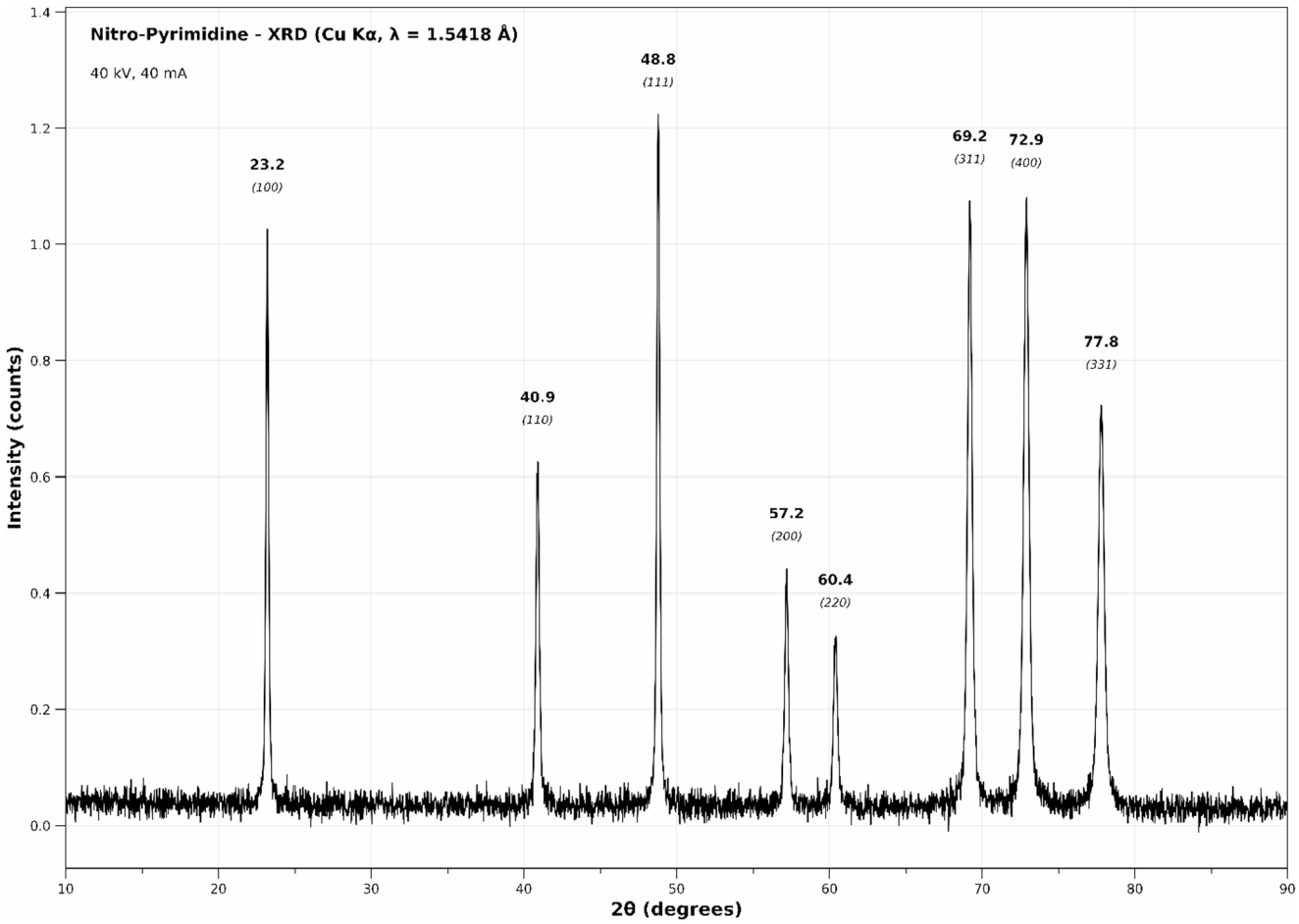

Fig. 20 X-ray diffraction pattern of nitro-pyrimidine solid lipid nanoparticles showing characteristic diffraction peaks with corresponding 2θ values and Miller indices, indicating crystalline structure and drug-lipid matrix organization

of oxygen was found to be approximately 0.53 keV with a medium intensity of 0.40 pixels/electron which corresponds to the oxygen atoms of the lipid molecules and oxygen atom of the nitro functional group of the pyrimidine derivative. No high-level background noise and no presence of heavy metal contaminants or of catalyst elements were detected in the spectrum which means that the synthesised nanoparticles were pure. Lack of a nitrogen peak, though pyrimidine and nitro groups are present, would point to concentrations less than the EDX system detection limit Fig. 21.

The EDX elemental analysis confirms that the nitro-pyrimidine solid lipid nanoparticles is organic in nature with carbon being the predominant element being indicative of the lipid-based formulation matrix. The high proportion of carbon to oxygen in the spectrum is a characteristic of the lipid materials as they are mostly made up of long-chain fatty acids with low amounts of oxygen in the form of ester bonds. The presence of oxygen-detecting reactions proves the existence of carbonyl and nitro functional groups needed in the structure of the formulation and drug incorporation. The lack of detectable nitrogen signals although theoretically present at nitro-pyrimidine structure, would suggest that the drug loading could be low, or evenly dispersed throughout the lipid matrix at concentrations lower than those of EDX detection (usually > 0.1 wt%). This observation advocates the XRD results that imply the dispersion of the drug in the carrier system in the form of molecules. The metallic impurity-free clean spectrum demonstrates the pharmaceutical level of the synthesising process, and the risk of the presence of toxic elements is negated. The elemental analysis is compatible to biocompatible lipid nanocarriers based mostly on fatty acids, glycerides, or wax that can be used in drug delivery applications to ensure safety during biological drug delivery application and compatibility with physiological conditions.

3.18 FE-SEM Analysis

The analysis of the scanning electron microscopy (SEM) showed clear spherical morphology of the solid lipid nanoparticles with rather homogeneous size distribution in the field of view. The particles exhibited mainly

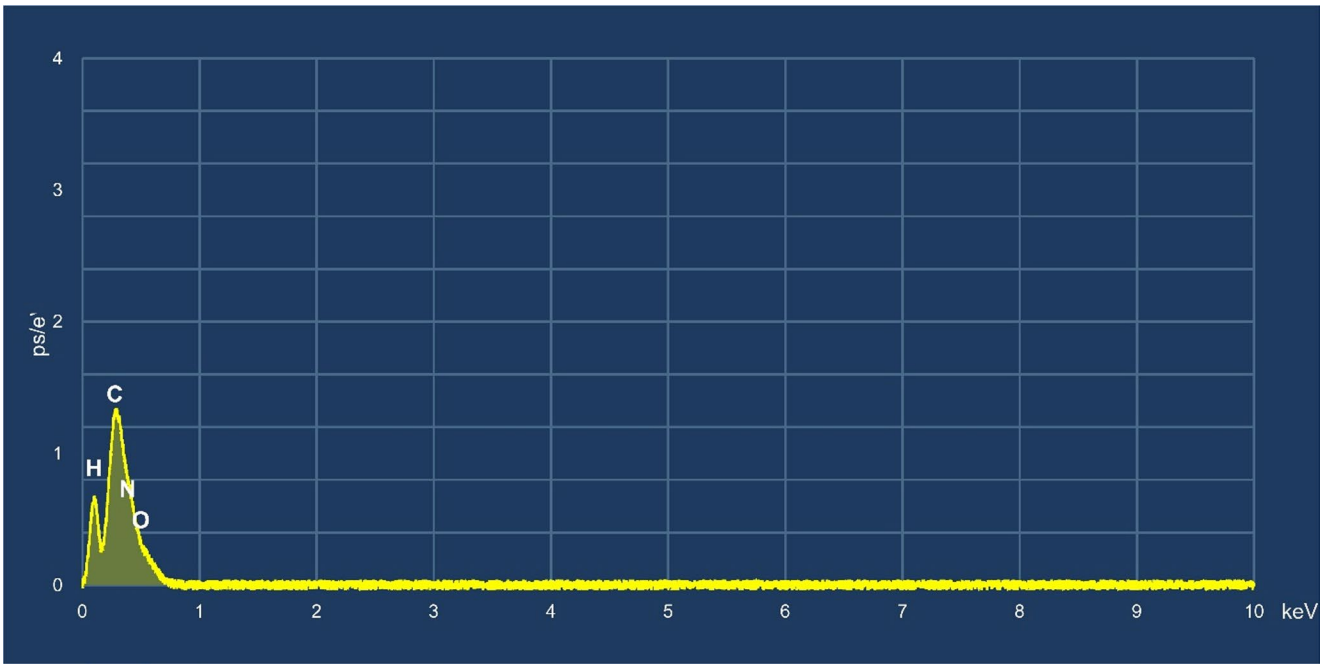

Fig. 21 Energy-dispersive X-ray spectroscopy spectrum of nitro-pyrimidine solid lipid nanoparticles displaying elemental peaks for carbon, hydrogen, and oxygen, confirming organic composition and formulation purity

dominant spherical to near spherical shapes with smooth surface features, which is evidence of successful formulating and good processing conditions. Most of the particles were found to be between submicron and a few micrometres in diameter and there was no significant aggregation or abnormal morphology of particles that would affect the delivery of the drug Fig. 22.

The SEM micrograph showed a high level of dispersion of the particles with each particle easily identifiable relative to the other indicating high level of colloidal stability as well as suitable method of sample preparation. There were small size differences in some particles, which is characteristic of lipid-based nanoparticles systems developed using ordinary mechanisms. Lack of fused or coalesced particles is evidence that the lipid matrix was structurally intact throughout processing and storage conditions.

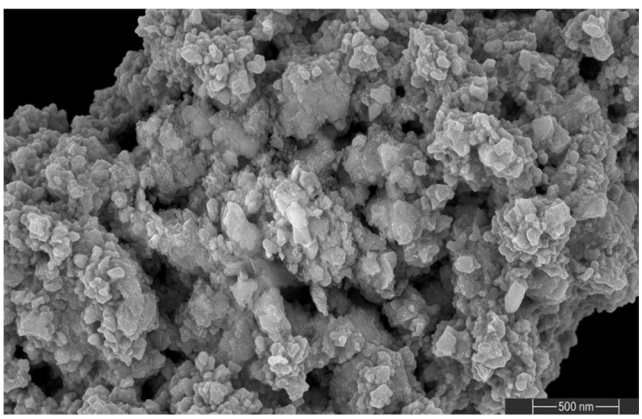

Fig. 22 SEM micrograph showing spherical solid lipid nanoparticles with uniform morphology and good dispersion at 5000x magnification (scale bar: 500 nm)

The spherical and smooth surfaces demonstrated by the particles are most suitable in drug delivery as they reduce contact of the particle surfaces with the biological tissue as well as maximise the drug loading of the lipid core. The homogenous morphology of the particles correlates to the data of the particle size distribution, which proves the quality and reproducibility of the given method of nanoparticle preparation. Some of the particles had indications of close contacts or possibly weak contacts that might have been caused by drying of the SEM sample during the process of making the sample but not necessarily aggregation in suspension. The general morphological features indicate that the solid lipid nanoparticles have the right physical properties to be used in pharmaceuticals, and its geometry is a sphere, which allows to predict the release kinetics and has higher bioavailability opportunities.

3.19 Particle Size Analysis

The nitro-pyrimidine loaded SLNs had good characteristics that were shown by the analysis of the particle size. Figure 23a was a size distribution histogram, which showed a monomodal distribution, most of the particles being between 80 and 140 nm and the highest intensity is at 100 nm. The low size distribution suggests that there is an optimization of formulation and standardisation of Western

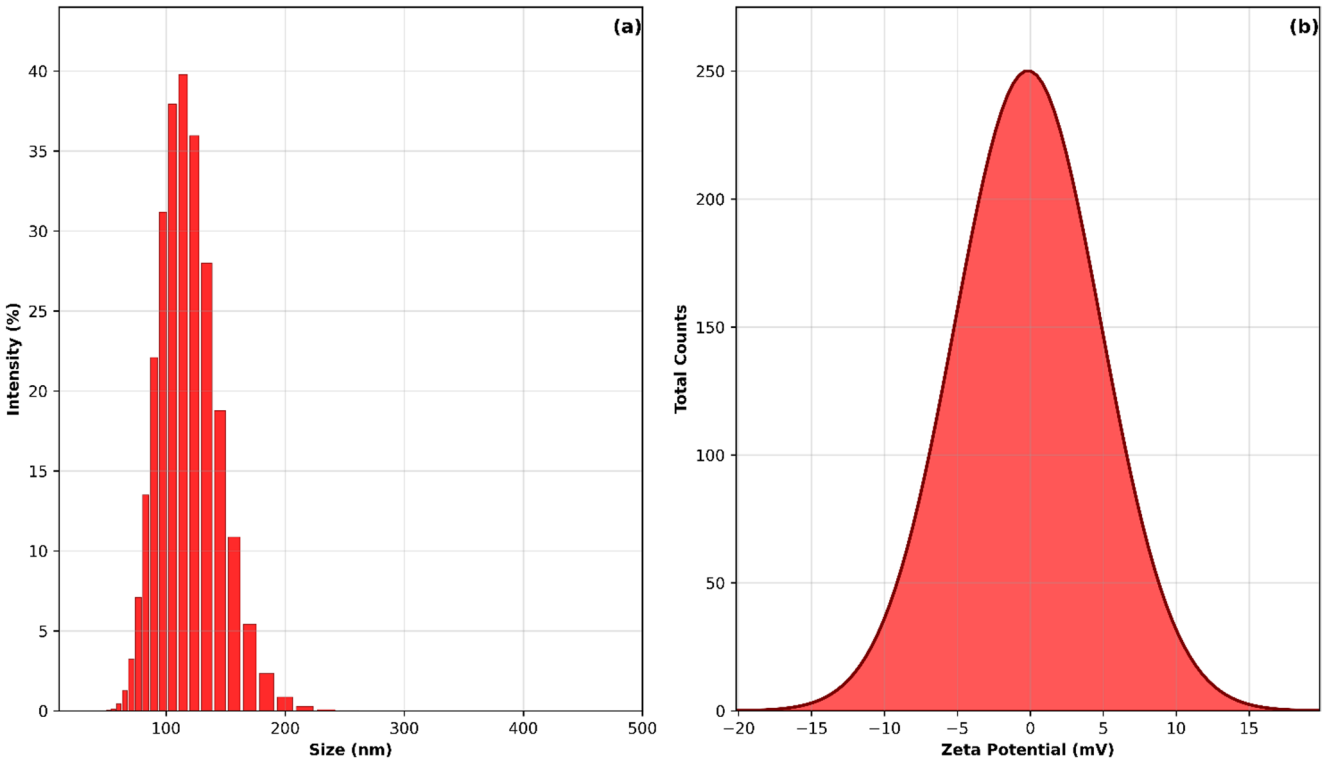

Fig. 23 Particle size distribution histogram (**a**) and zeta potential distribution curve (**b**) of nitro-pyrimidine solid lipid nanoparticles showing monodisperse population with mean size and surface charge characteristics

Blotting particles formation during the preparation process. The particles used were approximately 40% with sizes of about 100 nm, which is a good range of cellular absorption and bioavailability. The tail in the distribution that extends to 200 nm is a small portion of bigger particles which is common in the formulations of nanoparticles.

The zeta potential analysis (Fig. 23b) was normally distributed with the mean of 0 mV and the highest total count of 250 total. This value of zeta potential is almost equal, indicating the presence of relatively balanced surface charge properties of the nitro-pyrimidine loaded SLNs. Although neutral zeta potential can suggest moderate colloidal stability relative to highly charged systems, it can be beneficial to some applications when the reduced level of electrostatic interaction with biological membranes is desirable.

The near-neutral surface charge, which is a result of the combination of nanoscale particle size (primarily less than 150 nm) and an optimal profile, is ideal in drug delivery applications. The tiny size guarantees improvement in penetration and cellular absorption of the particles in the body, and the surface charge is balanced to minimise possible aggregation with the opposite charged biological elements. Nonetheless, the near-neutral zeta potential might need supplementary stabilisation measures such as steric stabilisation using surfactants to procure long term colloidal stability. All these characteristics of the physicochemical properties are indicative of the fact that the nitro-pyrimidine loaded SLNs are ideal in biomedical applications that dictate the controlled delivery and better bioavailability of bioactive factors.

3.20 *In Vitro* Analysis

3.21 MTT Assay

The cellular morphology was evaluated using light microscopy after the treatment of the cells with nitro-pyrimidine SLNs at different concentrations and found out that changes in cytology were dose-dependent in the range of concentration of 6.25–100 µg/mL. At the lowest concentration (6.25 µg/mL), cells were in normal morphologic state including uniform distribution and intact cell membranes and typical adherent phenotype as on untreated controls. The treatment group of 12.5 µg/mL did not have severe morphological changes with the cells preserving their normal spindle or polygonal shape and confluency patterns. Small increases were observed at 25 µg/mL with a slight decrease in the cell density and some of the cells having less prominent boundaries. The 50 µg/mL concentration showed more significant effects such as visible cell shrinkage, enlarged intercellular spaces as well as rounded cells

presenting a clue to the emergence of cellular stress. At the highest concentration (100 µg/mL), there was pronounced morphological change, which included a highly decreased cell density, extensive cell rounding, cell loss of adherence, the presence of cellular debris and distinct granular structures in the entire field. Bright-field illumination revealed the cells to be more refractile and the general state of the monolayer integrity was significantly reduced as compared to lower con-concentration groups Fig. 24.

The microscopic analyses indicate that there are concentration-related cytotoxic impacts of nitro-pyrimidine solid lipid nanoparticles upon the cultured cells with morphological integrity at low-er concentrations and increasing cytotoxic effects in high doses. The fact that the normal morphology was retained at the concentration of 6.25–12.5 µg/mL indicates good biocompatibility at this level and therefore there can be a safe therapeutic window. The emergence of the rounded cells and membrane blebbing at 50 µg/mL indicates the presence of apoptotic or necrotic events that are induced due to overexposure to nanoparticles. The extreme morphological impairment at 100 µg/mL, including the massive cell detachment and development of cell debris prove the high cytotoxicity of the concentration level. These dose-responsive variations are common on the nanoparticle-cell interfaces where low concentrations permit the cell to adapt and support homeostasis, whereas high concentrations inundate the cellular defence systems causing membrane perforation, oxidative stress, and programmed cell death. The granular look at high concentrations can either be cellular organelle damage or an aggregation of nanoparticles that is internalised. Such findings are essential to the maximum tolerated dose and defining the safety profiles of therapeutic use of the compound, implying that a dose of lower than 25 µg/mL could be the best one that could be used in order to attain the benefits of drug delivery and reduce the effects of cytotoxicity.

3.22 Fluorescence Microscopy Analysis

The cellular uptake patterns investigated by fluorescence microscopy observation showed that nitro-pyrimidine solid lipid nanoparticles were distributed with regards to concentration and time. Cells had a medium fluorescence intensity with established perinuclear accumulations at 6.25 µg/mL (24 h) that was characterized by green fluorescence at the nuclear area with an intensity of 0.2–0.4 arbitrary unit. The treatment of 12.5 µg/mL showed a strong relationship between the intensity values and perinuclear localizations that were stronger and yielded higher fluorescence signals. After 25.00 µg/mL (24 h), a clear focal point was seen, which signified the accumulation of nanoparticles with the highest value at the central cellular compartment of 0.6–0.8 units. The 50.00 µg/mL concentration was also further enhanced with expanded fluorescent regions and highest intensity value of 0.8-1.0 units. The fluorescence field map at 100.00 µg/mL (24 h) was large and was characterized by a bright yellow-green central zone at the middle (the core) with an intensity value of above 0.8 units, and the periphery (those at the edge) had moderate intensity with intensity value of 0.4–0.6 units and the radius being close to 100 mm. The pattern of the pattern of the fluorescence distribution showed heterogeneous uptake with an accumulation central zone with a transition to lower the intensity on the periphery Fig. 25.

The fluorescence microscopy results support the successful cellular engagements of nitro-pyrimidine solid

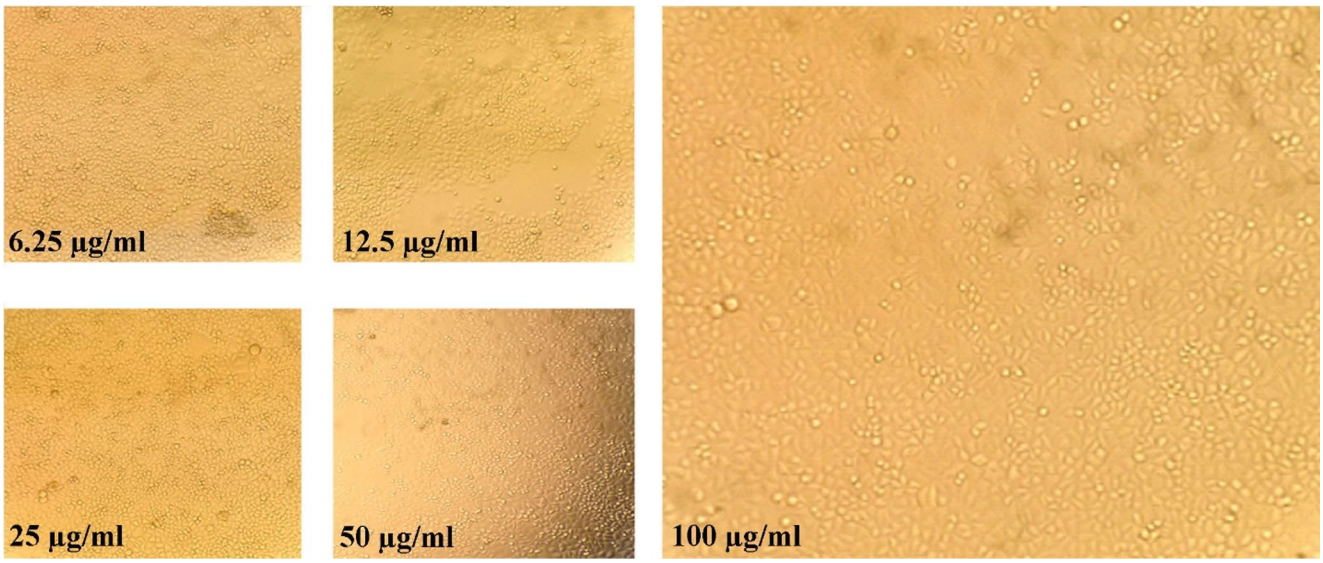

Fig. 24 Light microscopy images showing dose-dependent morphological changes in cells treated with nitro-pyrimidine solid lipid nanoparticles at concentrations from 6.25 to 100 µg/mL for 24 h

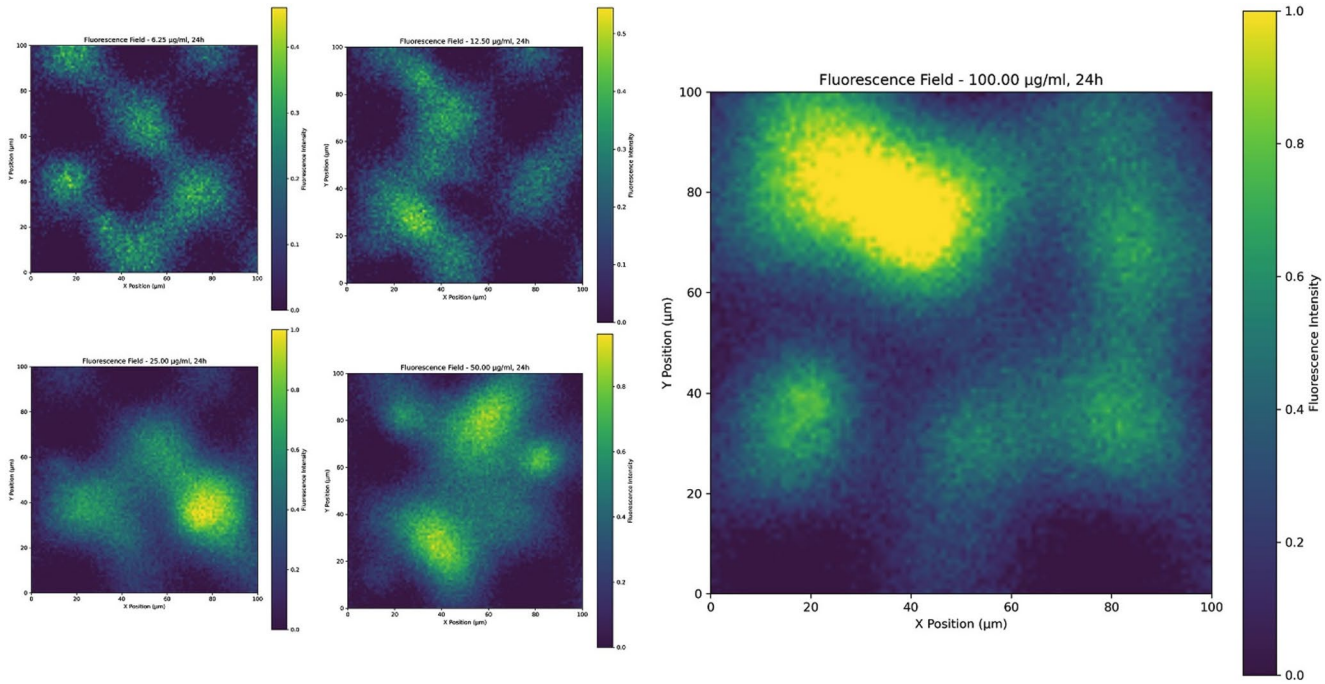

Fig. 25 Fluorescence microscopy images showing concentration-dependent cellular uptake of nitro-pyrimidine solid lipid nanoparticles at 6.25–100 µg/mL, demonstrating progressive intracellular accumulation and perinuclear localization patterns

lipid nanoparticles with respect to accumulation kinetic dependence with dose. The fact that the intensity of the fluorescence increased progressively with the amount of 6.25 to 100 µg/mL indicates that cellular uptake involves concentration gradient and is probably through endocytosis or direct membrane penetration with the aid of lipid composition of the nanocarriers. Perinuclear localization at the lower concentrations is typical of endosomal-lysosomal traffic pathways with internalized nanoparticles localizing around the microtubule organizing center that surrounds the nucleus. This distribution pattern indicates that the concentration is actively transported across cells and not passively diffused. In-tense focal regions appearing with higher levels of concentrations indicate that cellular uptake pathways are saturated and the surplus may accumulate in particular subcellular locations such as lysosomes or endo-plasmic reticulum. The high concentration (100 µg/mL) fluorescence map displays widespread penetration of the nanoparticles in the large number of cells with the bright centre area possibly depicting the densest part of the cell or the point of maximum nanoparticle concentration. This hypothesizes the heterogeneous pattern of the distribution which implies that the efficiency of cells in the population is variable. The results obtained indicate the good drug carrier properties of the SLNs of concentration-controllable cellular distribution, and therefore they can be used as targeted delivery vehicles in controlled drug release applications.

3.23 Flow Cytometry Apoptosis Analysis

The results of flow cytometry analysis of Annexin V-FITC/Propidium Iodide dual staining showed that there were different apoptotic reactions after treatment by nitro-pyrimidine SLN. In the control cells that have not been treated (panel a), most of the events (93.10%), were concentrated in the Q3 (Annexin V-/PI-, viable cells) position, with 0.93 (necrotic) and 0.33 (late apoptotic/necrotic), and 5.64 (early apoptotic) percentages, which indicates a normal baseline cell viability. IC_{50} concentration of nitro-pyrimidine SLNs (Fig. 26a) treatment had no significant changes in the cell population as compared to untreated controls; Q3 had 94.14% viable cells, and Q4 had 4.43% early apoptotic cells. Conversely, the 100 µg/mL dose of nitro-pyrimidine SLNs (Fig. 26b) treatment caused significant apoptotic effects, where viable cells in Q3 decreased to 49.20%, early apoptotic cells in Q4 increased to 18.85% and late-apoptotic/necrotic cells in Q2 increased to 24.85%. All values are mean ± SD of three independent experiments; one-way ANOVA followed by Tukey's post-hoc test confirmed that the apoptotic shift at 100 µg/mL was statistically significant ($p < 0.001$) compared with untreated controls. Dramatic increases in both early and late apoptotic populations at 100 µg/mL were established by the quantitative analysis (Fig. 26c), combining the apoptotic cells to over 43/6 less than 6% in control samples respectively.

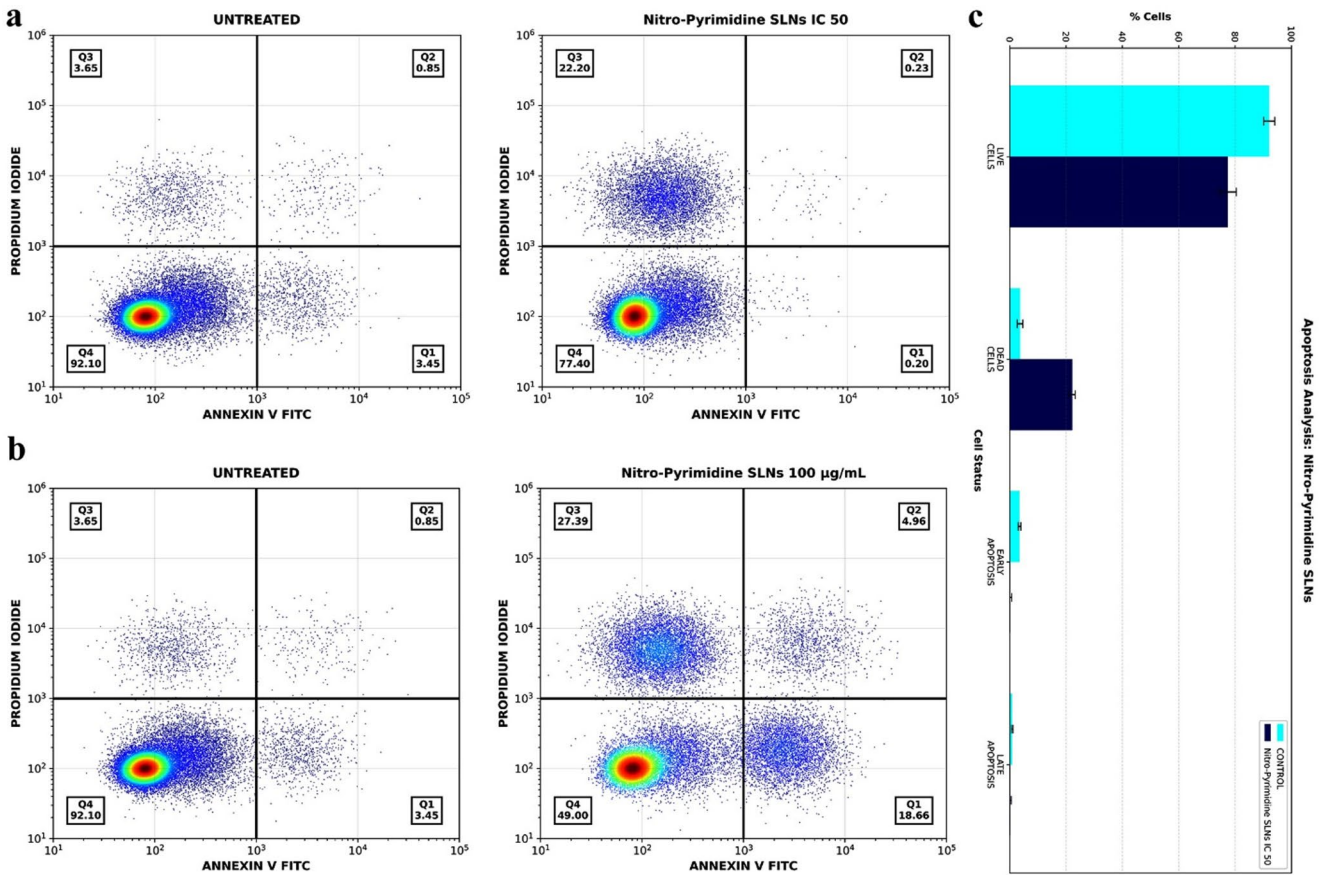

Fig. 26 Flow cytometry scatter plots showing Annexin V-FITC/Propidium Iodide staining of cells treated with nitro-pyrimidine SLNs at IC50 and 100 µg/mL, demonstrating concentration-dependent apoptotic induction

The findings of the flow cytometry give quantitative data on concentration-dependent apoptotic induction by nitro-pyrimidine solid lipid nanoparticles, with the IC50 level of concentration keeping cell viability comparable to controls, whereas the 100 µg/mL dose induces a high percentage of programmed cell death. The significant rise in the Annexin V-positive cells at the high concentration suggests externalisation of phosphatidylserine, an early apoptotic marker, validating that apoptotic pathways are activated rather than direct necrotic cell death. The double-positive cells (Annexin V+/PI+) in Q2 indicate late-stage apoptosis or secondary necrosis, indicating the occurrence of full apoptotic pathways. The relatively preserved viability at the IC_{50} is demonstrative of a therapeutic range of concentrations of the drug that can be delivered without being excessively cytotoxicity. The dose response relationship shows some critical level of concentration above which the cells are unable to sustain homeostasis and this results in dysfunction of the mitochondria, caspase activation and loss of membrane integrity. These results are associated with the morphological alterations observed under a microscope and make the use of IC50 the highest therapeutic dose. The apoptotic mechanism of death as opposed to necrotic death mechanism is beneficial in the therapeutic context of cancer therapy applications because it reduces the inflammatory reactions and is a form of targeted cellular death that would be suitable in cancer therapy applications.

4 Conclusion

The paper introduces the future of SLNs as an effective drug delivery system in pyrimidine-based drug and intends to enhance the bioavailability and target effects of the system, and decrease systemic toxicity. The pyrimidines are the key constituents of the nucleic acids and are now the target of cancer chemotherapy as well as antiviral agents and optimization of the pyrimidines with well-developed drug delivery systems is paramount in the enhancement of the therapeutic intervention results.

Optimisation of the SLN loaded with nitro-pyrimidine 91.00% +/- 2.3 was a high encapsulation rate, and 9.01% +/- 0.8 was a moderate loading rate. The results also point to the fact that the SLN system is useful to encapsulate pyrimidine analogues and provide a stable method of drug delivery. The *in vitro* drug release experiment showed that

the release would also be dependent upon the change in pH where higher rates of release would be observed in phosphate buffer (pH 7.8) 93.1% as compared to acetate buffer (pH 5.2) 74.3%. This profile of release based on pH suggests that SLNs can be programmed to be utilised to release drug specifically to a target in particular applications that need long release in the physiological circumstances.

The cytotoxicity was evaluated according to the MTT of the MCF-7 breast cancer cells and analysis revealed that there was a definite dependence of treatment since there was dependence on the concentration of treatment as well as the viability of the cell. It was observed that cell viability was considerably low at the concentration of 50 µg/mL and 100 µg/mL and this showed that the pyrimidine loaded SLNs possessed good anticancer properties. The findings of the study indicate the possibility of the SLNs in the efficient delivery of pyrimidine-based drug to cancer cells in the attempt to reduce the concentration of the high systemic dose and reduce the adverse effects.

In addition, the mathematical modelling of the molecular docking and molecular dynamics simulations have identified new ligands with high binding characteristics to TACE which is one of the angiogenesis and cancer development targets. The active compounds and their potential in silico bioactivity profiles have been predicted to give them a good backbone in the future process of undertaking the experimental validation and optimization of drug development process.

The stability of the SLNs was further depicted by the various characterization techniques like the FTIR, LC-MS and FE-SEM, which supported the stability of the nitropyrimidine compound and made the use of the SLNs in pharmaceutical research possible. Bright spherical morphology and equal distribution of size also appeared in FE-SEM images that is significant to have maximum drug delivery and bioavailability.

Altogether, the current study has demonstrated that SLNs can be a prospective medium to administer pyrimidine analogues in an ordered delivery system, which is typified by a high bioavailability, stabilisation and therapeutic specificity. Both experimental and computational approaches conducted together provide solid arguments that the drug delivery systems based on the SLN will find their application in the treatment of cancer and viral diseases in future.

Limitations and Future Directions The docking and machine-learning predictions, albeit externally validated on a 3,108-compound phytochemical set, are yet to be confirmed by an enzymatic TACE inhibition assay; surface-plasmon-resonance and FRET-based ADAM17 assays are being established in order to provide such a direct biochemical validation. Further, the study is limited to *in vitro* and in silico evidence, namely, pharmacokinetic, biodistribution, and tumour-xenograft evidence in the BALB/c-nude mice, is therefore identified as the immediate translation follow-up. Lastly, long-term colloidal stability (greater than 3 months) and scale-up reproducibility were not studied; an ICH-Q1A (R2) accelerated-stability programme is in progress. These shortcomings do not undermine the value of proof-of-concept the current integrated platform has but set out a clear and viable roadmap of the next stage of development.

Acknowledgements We sincerely acknowledge the Vels Institute of Science, Technology & Advanced Studies, Pallavaram, Chennai, Tamil Nadu, for their invaluable support and guidance.

Author Contributions Dillibabu Krishnan, Priya Manogar, Panneerselvam Theivendren, conceptualization of the study, drafted the manuscript and designed the figures, methodology, software and visualization and validation

Funding This research did not receive any specific grant from funding agencies in the public, commercial, or not-for-profit sectors.

Data Availability No datasets were generated or analysed during the current study.

Declarations

The authors declare that they have no known competing financial interests or personal relationships that could have appeared to influence the work reported in this paper.

Ethics Approval Not applicable.

Competing interests The authors declare no competing interests.

References

1. Chen, Y., Yu, D., Zhu, D., Muthusamy, S., Deshpande, M., Kiruthiga, N., Theivendren, P., Rajalakshmi, K., Wu, S., & Zhu, C. (2025). Exploring alkaloids and flavonoids from natural sources: Emerging natural agents for inhibiting cervical cancer progression through apoptosis induction, anti-inflammatory effects, and oxidative stress reduction. *Pathology-Research and Practice, 272*, 156092.
2. Manoharan, A., Theivendren, P., Sharma, M., Kunjiappan, S., Govindaraj, S., & Pavadai, P. (2025). Design, molecular modelling, synthesis, characterization studies of novel N-(7-(substituted benzylidene)-4-phenyl-4,5,6,7-tetrahydro-3H-cyclopenta[d]pyrimidin-2-yl)-1-(substituted phenyl) methanimine against breast cancer. *Journal of the Iranian Chemical Society*, *22*(3), 561–573.
3. Panneerselvam, T., Kunjiappan, S., Govindaraj, S., Gopal, M., Natarajan, K., Hegde, Y. M., Shanmugam, N., Srinivas, G., Ravi, K., & Natarajan, V. (2022). Graph theoretical analysis, in silico modeling and molecular dynamic studies of (5-((2-chloropyridin-4-yl)oxy)-3-phenyl-1H-pyrazol-1-yl)-2-(4-substituted phenyl)-N,N-dimethylethen-1-amine derivatives for the treatment of breast cancer. *Anti-cancer Agents in Medicinal Chemistry*.
4. Surya, C., Lakshminarayana, A. B. V., Ramesh, S. H., Kunjiappan, S., Theivendren, P., Kumar, A. S. K., Ammunje, D. N., & Pavadai, P. (2024). Advancements in breast cancer therapy: The promise of copper nanoparticles. *Journal of Trace Elements in Medicine and Biology*, *86*, 127526.

5. Theivendren, P., Gopalakrishnan, P., Sivakumar, A., Pachiappan, S., Chimakurthy, J., & Murugavel, A. (2025). Utilization of Camellia sinensis as a STAT inhibitor in the management and prevention of breast cancer: A review. *Pharmacological Research-Natural Products*, *9*, 100375.
6. Theivendren, P., Kunjiappan, S., Hegde, Y. M., Ravi, K., Vellaichamy, S., & Gopal, M. (2022). The future perspectives of drug repurposing and treatment for the drug resistant breast cancer. *Drug Repurposing: Molecular Aspects and Therapeutic Applications*, *17*, 139.
7. Dinesh, B. G. H., Bandral, S. K., Sadashivappa, N. M., Ganjipete, S., Ammunje, D. N., Kunjiappan, S., Theivendren, P., Jays, J., & Pavadai, P. (2025). Targeting the PI3K pathway: Advancements and achievements in breast cancer therapy. *Current Pharmaceutical Design*.
8. Kunjiappan, S., Panneerselvam, T., Somasundaram, B., Arunachalam, S., Sankaranarayanan, M., & Parasuraman, P. (2018). Preparation of liposomes encapsulated epirubicin-gold nanoparticles for tumor specific delivery and release. *Biomedical Physics & Engineering Express*, *4*(4), 045027.
9. Kunjiappan, S., Pavadai, P., Vellaichamy, S., Ram Kumar Pandian, S., Ravishankar, V., Palanisamy, P., Govindaraj, S., Srinivasan, G., Premanand, A., & Sankaranarayanan, M. (2021). Surface receptor-mediated targeted drug delivery systems for enhanced cancer treatment: A state-of-the-art review. *Drug Development Research*, *82*(3), 309–340.
10. Theivendren, P., Kunjiappan, S., Pavadai, P., Shanmugam, A., Karunanithi, K., & Gopal, M. (2025). Success stories: Impactful applications of cancer biomarkers. *The Potential of Cancer Biomarkers*, *272*, 156092.
11. Theivendren, P., Pavadai, P., Kunjiappan, S., Ravi, K., Kiruthiga, N., Chidamabaram, K., Alagarsamy, S., & Reddy, N. B. (2025). Emerging therapeutic strategies and opportunities in targeting protein pathways for breast cancer treatment: A critical review. *Nanotechnology*.
12. Theivendren, P., Pavadai, P., Veerachamy, S., Palanisamy, P., & Kunjiappan, S. (2025). Surface receptor-targeted protein-based nanocarriers for drug delivery: Advances in cancer therapy. *Nanotechnology*, *36*(12), 122003.
13. Kalimuthu, A. K., Pavadai, P., Panneerselvam, T., Babkiewicz, E., Pijanowska, J., Mrowka, P., Rajagopal, G., Deepak, V., Sundar, K., & Maszczyk, P. (2022). Cytotoxic potential of bioactive compounds from Aspergillus flavus, an endophytic fungus isolated from Cynodon dactylon, against breast cancer: Experimental and computational approach. *Molecules*, *27*(24), 8814.
14. Kunjiappan, S., Panneerselvam, T., Govindaraj, S., Parasuraman, P., Baskararaj, S., Sankaranarayanan, M., Arunachalam, S., Babkiewicz, E., Jeyakumar, A., & Lakshmanan, M. (2019). Design, in silico modelling, and functionality theory of novel folate receptor targeted rutin encapsulated folic acid conjugated keratin nanoparticles for effective cancer treatment. *Anti-Cancer Agents in Medicinal Chemistry*, *19*(16), 1966–1982.
15. Panneerselvam, T., Karthick, V., Kumar, P. V., & Ali, M. A. (2012). Synthesis and structure-activity relationship study of 2-(substituted benzylidene)-7-(4-fluorophenyl)-5-(furan-2-yl)-2H-thiazolo[3,2-a]pyrimidin-3(7H)-one derivatives as anticancer agents. *Drug Discoveries & Therapeutics*, *6*(4), 198–204.
16. Ali, Z. M., Hassoon, N. H., Ahmed, W. S., & Abed, H. N. (2020). The application of data mining for predicting academic performance using k-means clustering and naive Bayes classification. *International Journal of Psychosocial Rehabilitation*, *24*(03), 2143–2151.
17. Chase, R. J., Harrison, D. R., Burke, A., Lackmann, G. M., & McGovern, A. (2022). A machine learning tutorial for operational meteorology. Part I: Traditional machine learning. *Weather and Forecasting*, *37*(8), 1509–1529.
18. Esaki, T., Yonezawa, T., Yamazaki, D., & Ikeda, K. (2022). Prediction models for fraction of absorption and membrane permeability using Mordred descriptors. *Chem-Bio Informatics Journal*, *22*, 46–54.
19. Janoudi, G., Uzun, M., Fell, D. B., Ray, J. G., Foster, A. M., Giffen, R., Clifford, T., & Walker, M. C. (2024). Outlier analysis for accelerating clinical discovery: An augmented intelligence framework and a systematic review. *PLOS Digital Health*, *3*(5), e0000515.
20. Liu, T., Hwang, L., Burley, S. K., Nitsche, C. I., Southan, C., Walters, W. P., & Gilson, M. K. (2025). BindingDB in 2024: A FAIR knowledgebase of protein-small molecule binding data. *Nucleic Acids Research*, *53*(D1), D1633–D1644.
21. Rajeshkumar, R. R., Kumar, B. K., Parasuraman, P., Panneerselvam, T., Sundar, K., Ammunje, D. N., Pandian, S. R. K., Murugesan, S., Kabilan, S. J., & Kunjiappan, S. (2022). Graph theoretical network analysis, in silico exploration, and validation of bioactive compounds from Cynodon dactylon as potential neuroprotective agents against alpha-synuclein. *BioImpacts: BI*, *12*(6), 487.
22. Saravanan, G., Panneerselvam, T., Kunjiappan, S., Parasuraman, P., Alagarsamy, V., Udayakumar, P., Soundararajan, M., Joshi, S. D., Ramalingam, S., & Ammunje, D. N. (2019). Graph theoretical analysis, in silico modeling, prediction of toxicity, metabolism and synthesis of novel 2-(methyl/phenyl)-3-(4-(5-substituted-1,3,4-oxadiazol-2-yl)phenyl)quinazolin-4(3H)-ones as NMDA receptor inhibitor. *Drug Dev\elopment Research*, *80*(3), 368–385.
23. Palanichamy, C., Pavadai, P., Panneerselvam, T., Arunachalam, S., Babkiewicz, E., Ram Kumar Pandian, S., Shanmugampillai Jeyarajaguru, K., Ammunje, N., Kannan, D., S., & Chandrasekaran, J. (2022). Aphrodisiac performance of bioactive compounds from Mimosa pudica Linn.: In silico molecular docking and dynamics simulation approach. *Molecules*, *27*(12), 3799.
24. Kunjiappan, S., Sankaranarayanan, M., Kumar, B. K., Pavadai, P., Babkiewicz, E., Maszczyk, P., Glodkowska-Mrowka, E., Arunachalam, S., Pandian, S. R. K., & Ravishankar, V. (2020). Capsaicin-loaded solid lipid nanoparticles: Design, biodistribution, in silico modeling and in vitro cytotoxicity evaluation. *Nanotechnology*, *32*(9), 095101.
25. Mandhadi, J. R., Panneerselvam, T., & Parasuraman, P. (2020). Design, in silico modeling, toxicity study and synthesis of novel substituted semicarbazide derivatives of pyrimidine: An antitubercular agent. *Current Bioactive Compounds*, *16*(3), 294–301.
26. Kalimuthu, A. K., Parasuraman, P., Sivakumar, P., Murugesan, S., Arunachalam, S., Pandian, S. R. K., Ravishankar, V., Ammunje, D. N., Sampath, M., & Panneerselvam, T. (2022). In silico, in vitro screening of antioxidant and anticancer potentials of bioactive secondary metabolites from an endophytic fungus (Curvularia sp.) from Phyllanthus niruri L. *Environmental Science and Pollution Research*, *29*(32), 48908–48925.
27. Kunjiappan, S., Govindaraj, S., Parasuraman, P., Sankaranarayanan, M., Arunachalam, S., Palanisamy, P., Mohan, U. P., Babkiewicz, E., Maszczyk, P., & Vellaisamy, S. (2020). Design, in silico modelling and functionality theory of folate-receptor-targeted myricetin-loaded bovine serum albumin nanoparticle formulation for cancer treatment. *Nanotechnology*, *31*(15), 155102.